Published in final edited form as:

Nature. 2024 March ; 627(8002): 165–173. doi:10.1038/s41586-023-06993-7.

Identification of direct connections between the dura and the brain

Leon CD Smyth[1,2,#], **Di Xu**[1,2,*], **Serhat V Okar**[3,*], **Taitea Dykstra**[1,2], **Justin Rustenhoven**[1,2,4,5], **Zachary Papadopoulos**[1,2,6], **Kesshni Bhasiin**[1,2], **Min Woo Kim**[1,2,7], **Antoine Drieu**[1,2], **Tornike Mamuladze**[1,2,7], **Susan Blackburn**[1,2], **Xingxing Gu**[1,2], **María I Gaitán**[3], **Govind Nair**[8], **Steffen E Storck**[1,2], **Siling Du**[1,2,7], **Michael A White**[9], **Peter Bayguinov**[10,11], **Igor Smirnov**[1,2], **Krikor Dikranian**[11], **Daniel S Reich**[3], **Jonathan Kipnis**[1,2,6,7,#]

[1]Brain Immunology and Glia (BIG) Center, Washington University in St. Louis, St. Louis, MO, 63110, USA.

[2]Department of Pathology and Immunology, School of Medicine, Washington University in St. Louis, St. Louis, MO, 63110, USA.

[3]Translational Neuroradiology Section, National Institute of Neurological Disorders and Stroke, National Institutes of Health, Bethesda, MD 20892, USA.

[4]Department of Pharmacology and Clinical Pharmacology, Faculty of Medical and Health Sciences, University of Auckland, 85 Park Road, Grafton, Auckland, 1023, New Zealand.

[5]Centre for Brain Research, Faculty of Medical and Health Sciences, University of Auckland, Auckland, New Zealand.

[6]Neuroscience Graduate Program, School of Medicine, Washington University in St. Louis, St. Louis, MO, 63110, USA.

[7]Immunology Graduate Program, School of Medicine, Washington University in St. Louis, St. Louis, MO, 63110, USA.

[8]Quantitative MRI Core Facility, National Institute of Neurological Disorders and Stroke, National Institutes of Health, Bethesda, MD 20892, USA.

[#]Correspondence should be addressed to LCDS (l.c.smyth@wustl.edu) or JK (kipnis@wustl.edu).
[*]These authors contributed equally

Author contributions

L.S. designed and performed experiments, analyzed, and interpreted data, created the figures and wrote the manuscript. D.X. designed and performed experiments, analyzed, and interpreted data. S.V.O., M.I.G., and G.N. performed MRI experiments, processed, and analyzed images, and wrote relevant methods sections. T.D. performed the scRNA-seq data analyses and assisted in writing relevant methods. J.R. designed and performed experiments and provided intellectual contributions. Z.P. assisted with tissue clearing, light sheet imaging, and 3D visualization. M.W.K. performed EAE experiments and scored EAE mice in a blinded manner. A.D. assisted with CSF tracer imaging experiments and co-discovered the perivenous CSF efflux route. T.M. designed experiments and provided intellectual contributions. K.B., S.B., and X.G. assisted in harvesting, staining, and imaging tissues. S.E.S. provided intellectual contributions. K.B. assisted in harvesting, staining, and imaging tissues. S.D. performed staining and imaging of human dura-arachnoid granulation specimens. M.A.W. assisted in the design and generation of the novel transgenic mice. P.B. assisted in 2P imaging. I.S. performed animal surgeries. K.D. assisted with interpretation and analysis of electron microscopy images. D.S.R. designed MRI studies, led and provided resources related to MRI studies, and provided intellectual contribution. J.K. designed the experiments, provided resources and intellectual contribution, oversaw data analysis and interpretation, and wrote the manuscript.

Competing interest statement

J.K is a co-founder of Rho Bio.

[9]Department of Genetics, Washington University School of Medicine, Washington University in St. Louis, St. Louis, MO 63110, USA.

[10]Washington University Center for Cellular Imaging, Washington University School of Medicine, Washington University in St. Louis, St. Louis, MO 63110, USA.

[11]Department of Neuroscience, Washington University School of Medicine, Washington University in St. Louis, St. Louis, MO 63110, USA.

Abstract

The arachnoid barrier delineates the border between the central nervous system and dura mater. Although the arachnoid barrier creates a partition, communication between the central nervous system and the dura mater is crucial for waste clearance and immune surveillance [1,2]. How the arachnoid barrier balances separation and communication is poorly understood. Leveraging transcriptomic data, we developed novel transgenic mice to examine specific anatomical structures that serve as routes across the arachnoid barrier. Bridging veins create discontinuities where they cross the arachnoid barrier, forming structures that we termed arachnoid cuff exit (ACE) points. The openings that ACE points create allow the exchange of fluids and molecules between the subarachnoid space and the dura, enabling the drainage of cerebrospinal fluid and limited entry of molecules from the dura to the subarachnoid space. In healthy human volunteers, MRI tracers transit along bridging veins in a similar fashion to access the subarachnoid space. Interestingly, in neuroinflammatory conditions such as experimental autoimmune encephalomyelitis, ACE points also allow cellular trafficking, representing a previously unknown route for immune cells to directly enter the subarachnoid space from the dura mater. Collectively, our results indicate that ACE points are a critical part of the anatomy of neuroimmune communication in both mice and humans that links the central nervous system with the dura and its immunological diversity and waste clearance systems.

Introduction

The central nervous system (CNS) is surrounded a series of barriers that were historically thought to completely prevent its interaction with the peripheral immune system and contribute to its immune privilege [3]. The most well-studied of these is the blood-brain barrier, formed by the endothelial cells of the brain [3]. The other is the blood-cerebrospinal fluid (CSF) barrier, which has two anatomical components, the choroid plexus epithelium in the ventricles that filters fluid from the choroid plexus stroma to produce CSF, and the arachnoid barrier in the meninges which forms the boundary between the dura mater and the subarachnoid space . The flow of CSF within the subarachnoid space and through the brain has been proposed to be important to the clearance of brain wastes and antigens [4]. Historically, it was thought that arachnoid granulations, outpouchings of the arachnoid mater into the venous sinuses of the dura mater, allowed drainage of CSF directly to the bloodstream [5]. This drainage mechanism was proposed to keep the peripheral immune system ignorant to CNS antigens, however, no *in vivo* evidence exists that granulations participate in CSF drainage [6].

On the other hand, it is well-established that tracers injected into the CNS or the CSF drain to cervical lymph nodes [7,8], indicating that, despite the presence of these barriers, the peripheral immune system constantly surveils the brain. Drainage of CSF around nerve sheaths and to extracranial lymphatics has been proposed as one mechanism through which drainage of CSF can occur [9,10]. More recently, bona fide lymphatic vasculature has been identified in the dura mater, and, in addition to draining dural molecules, is capable of draining CSF which enters the dura mater [1,1,8,11–14]. The efflux of CSF to the dura mater is not only important for the drainage of wastes, but also the presentation of antigens, negative selection of B cells, and communication with the adjacent skull bone marrow [2,15,16]. On the other hand, immune cells in the dura mater and the cytokines that they produce have been proposed to play a role in shaping behavior [17,18]. Supporting this notion, transcranially applied tracers can be found in the brain and transcranial IL-6 enhances recovery following cerebral vascular injury [19,20]. Finally, the leptomeninges is a critical site of immune infiltration in neuroinflammatory diseases, including multiple sclerosis [21], metastatic brain tumors [22–24], and infectious meningitis [25–29]. The mechanism that enables this communication between the dura mater and subarachnoid space has not yet been described.

Here, we profiled the functional anatomy of the arachnoid barrier. We performed single nuclei RNA-sequencing (snRNA-seq), electron microscopy, and tracer studies to characterize the barrier properties of the leptomeningeal stroma. Leveraging our transcriptomic data, we identified existing mice for the visualization and genetic manipulation of the leptomeninges, and developed two novel mouse strains for the targeting of ABCs and dural border cells (DBCs). Using these, we identified discontinuities in the arachnoid barrier around bridging veins, which we term arachnoid cuff exit (ACE) points. ACE points permit the exchange of tracers between the dura mater and the subarachnoid space, enabling the clearance of CSF tracers. Furthermore, ACE points act as a route for immune cells to enter the subarachnoid space in neuroinflammatory disease. We propose that ACE points are specialized regions of the arachnoid mater that are important in brain waste clearance and neuroimmune communication.

The route of CSF efflux is controversial. It has been proposed that CSF drains directly into the blood through arachnoid granulations, around nerve sheaths to extracranial lymphatics [9], and to the dura to be drained by meningeal lymphatics [1,2,14]. We initially wanted to determine if i.c.m. tracers reach the dura mater indirectly, through efflux to blood. To test this, we injected tracers i.v. or i.c.m., then examined the dura mater. If i.c.m. tracers reached the dura by blood, they would be expected to mimic the distribution of i.v. tracers. However, we observed strikingly different distribution of tracers, with i.v. tracers spread throughout the dura, while i.c.m. tracers were confined to the regions around the venous sinuses (Extended data Fig. 1a–e). Tracers injected i.c.m. accumulated prominently around ‘hot-spots’ – bilaterally at the transverse sinus and around where the rostral rhinal vein joins the superior sagittal sinus (Extended data Fig. 1a) [2,14]. We then interrogated the kinetics of i.c.m. tracers in perisinus regions, cervical lymph nodes, and the femoral vein. We observed that the appearance of tracers in perisinus regions preceded the appearance in both the cervical lymph nodes and the blood (Extended data Fig. 1f–i, Supplementary video 1). Because transcranial imaging cannot distinguish between the subarachnoid and

dural compartments, we confirmed that tracers reached the dura mater prior to appearance in the lymphatic system and blood by measuring the concentration of tracers in lysates from the brain, dura, cervical lymph nodes, and serum (Extended data Fig. 1j–n). Because we detect tracers in the dura prior to detecting them in other compartments we concluded that CSF efflux to the dura was direct. We further found that tracers of multiple molecular weights and properties, including dextrans (10, 70, 2000 kDa), ovalbumin (45 kDa), and 0.5 μm polystyrene beads, appear in the dura at the same rate, suggestive of bulk efflux (Extended data Fig. 1o–q). Collectively, these results informed a working model for CSF efflux where CSF accesses the dura mater *directly* through bulk flow before it can be drained by conventional lymphatics (Fig. 1a).

Because the arachnoid barrier separates the dura mater from the subarachnoid space, we hypothesized that this barrier plays a key role in CSF efflux to the dura (Fig. 1a–c). We initially proposed that this may occur through specialized transport functions of arachnoid barrier cells (ABCs). ABCs make up a small proportion of the total cells in the brain because they are only found at the very edge of the brain in a thin layer (Fig. 1b,c). Furthermore, no reliable protocols exist to enrich ABCs for sequencing, and as such have been poorly captured in whole brain sequencing datasets. We therefore peeled the leptomeninges from the brain and performed unbiased snRNA-seq to profile transport functions of ABCs that may enable direct efflux of tracers to the dura mater (Fig. 1d, Extended data Fig. 2a). We captured 31,346 nuclei, including 1,871 ABCs (Fig 1d, Supplementary table 1). Additionally, we detected expected populations of leptomeningeal stromal cells including pial and arachnoid fibroblasts (11,092 cells), dural border cells (DBCs; 8,600 cells), venous and arterial endothelial cells (2,876 cells), pericytes (327 cells), vascular smooth muscle cells (932 cells), macrophages (1,341 cells), T cells (435 cells), monocytes (528 cells) and dendritic cells (396 cells), as well as smaller populations of brain cell types including recently identified glia limitans superficialis astrocytes (Fig. 1d, Supplementary table 1) [30]. We validated the assignment of these clusters with RNAscope and immunolabeling (Extended data Fig. 2b–k). ABCs expressed known markers including *Cldn11*, *Cdh1*, *Klf5*, and *Cd55* (Extended data Fig. 2b, Supplementary table 2) [27,31,32]. We further identified markers including *Dpp4*, *Slc7a14*, *Msln*, *Cubn*, and *Sema3d* (Extended data Fig. 2b,e–f, Supplementary table 2). Based on gene ontology analysis of ABC markers, we did not detect enrichment of transport processes, with most of the transcriptome devoted to cytoskeletal and junction formation processes (Fig. 1e). Furthermore, we did not detect any ABC subclusters that had enrichment for fluid transport processes (Extended data Fig. 2l,m). Finally, comparison of ABCs with core gene sets for cell types indicated that they are similar to other barrier-forming cell types, including mesothelial and epithelial cells, as well as fibroblasts (Extended data Fig. 2n–q).

We performed immunostaining and electron microscopy (EM) of tight junctions and vesicles in ABCs to determine potential paracellular or transcellular pathways across the arachnoid barrier. We observed only sparse vesicles in ABCs by electron microscopy indicating that their capacity for transcytosis is limited (Extended data Fig. 3a–d). To overcome the limitations of assessing transport in static images we performed intravital imaging of the uptake of i.c.m. tracers. Previous work has shown that macrophages uptake CSF tracers [33,34], and we likewise observe the majority of tracer uptake by macrophages and

not in ABCs (Extended data Fig. 3e–f, Supplementary video 2). As suggested by gene ontology analysis, we observed high expression of junction components, with unique junctional organization in ABCs (Extended data Fig. 3g). ABC junctions were continuous and ubiquitous, and we did not observe zipper or button junctions which would enable exchange of fluid (Extended data Fig. 3h–j).

Research on the arachnoid barrier, and leptomeninges in general, has been hampered by a lack of genetic tools for the targeting of ABCs and leptomeningeal stroma. We therefore leveraged our sequencing data to determine if any existing mouse models may target ABCs or arachnoid-associated cells. We identified *Prox1*-EGFP, which has been previously shown to label a putative fourth layer of the meninges, the subarachnoid lymphatic-like membrane (SLYM) [35], as enriched in arachnoid-zonated FBs (Extended data Fig. 4a–c) We confirmed the presence of Prox1-positive cells beneath ABCs using confocal microscopy and flow cytometry (Extended data Fig. 4a–e). These results also agree with two other recent reports showing that Prox1 labels a layer of fibroblasts within the subarachnoid space [32,36]. We also found that *Cdh5*, a well-established marker of endothelial cells, was also expressed in ABCs, DBCs, and pial and arachnoid fibroblasts in our sequencing dataset (Extended data Fig. 4a–c). We confirmed that this represented real expression with immunolabeling and in *Cdh5*-CreER^{T2}::tdTom mice, where we observed recombination in endothelial cells, as well as recombination in DBCs, pial and arachnoid FBs, and ABCs (Extended data Fig. 2f, Extended data Fig. 4a–e). Importantly, the expression of Cdh5 in the pia and arachnoid mater has recently been confirmed in an independent reporter model [9,36].

Neither of these tools, however, provides specific targeting of leptomeningeal populations. We developed a *Dpp4*-CreER^{T2} mouse to target ABCs, because it was the top signature gene for ABCs and based on IHC of the brain, was specific to ABCs (Fig. 1f, Extended data Fig. 2b, e–f). When crossed to a reporter, we observed recombination in polygonal cells on the brain surface (Extended data Fig. 4f,g), which we confirmed were ABCs by confocal microscopy (Fig. 1g). We determined that the insertion of the CreER^{T2} cassette did not disrupt expression of endogenous *Dpp4* in *Dpp4*-CreER^{T2} heterozygous animals (Extended data Fig. 4h). We also developed a *Slc47a1*-CreER^{T2} based on its expression within putative DBCs (Fig. 1h, Extended data Fig. 2b,d). We confirmed recombination of this gene in the leptomeninges in irregularly shaped cells, which sat above the ABC layer in the expected location of DBCs (Fig. 1i, Extended data Fig. 4i,j). We also saw extensive recombination throughout the dura mater, particularly around the sinuses and tentorial folds, as expected for a dural-associated cell type (Fig. 1i). As with *Dpp4*, the insertion of the CreER^{T2} cassette did not disrupt endogenous expression of *Slc47a1* (Extended data Fig. 4k). We further used the *Dpp4*-CreER^{T2}::zsGreen mice to confirm the lack of uptake of i.c.m. injected tracers with intravital two-photon imaging (Extended data Fig. 4l, Supplementary video 3).

While examining the dura mater of *Dpp4*-CreER^{T2}::zsGreen reporter mice, we noted that bridging veins, which drain blood from the brain into the sinuses (Fig. 2a), had extensive coverage by zsGreen-positive ABCs (Fig. 2b). We confirmed this with three antibodies for ABCs: E-Cadherin, Cldn11, and Dpp4 (Fig. 2b). Bridging veins run through the subarachnoid space but must puncture the arachnoid barrier to drain into the sinus. At these points we hypothesized that ABCs were incapable of forming a seal, and instead

form a cuff around the vein. We termed these arachnoid cuff exit (ACE) points. We extensively characterized the stromal environment of ACE points, and find that they contained DBCs, arachnoid FBs, Prox1-positive FBs, but not pial FBs (Extended data Fig. 5a–k, Supplementary video 4–7). We also confirmed that ACE points formed cuffs using intravital imaging, and that these are not sealed onto either side of the vein, creating a potential space of the exchange of solutes between the dura and the subarachnoid space (Extended data Fig. 5j, Supplementary video 6). Furthermore, we observed a sharp transition of endothelial cells at ACE points from a BBB phenotype (GLUT1 and Cldn5-positive) to a peripheral (PLVAP-positive) phenotype indicating that the BBB is intact until the bridging vein has exited the ACE point (Extended data Fig. 5l–n).

Because the arachnoid barrier did not fully seal at ACE points, we speculated that these may allow CSF efflux to the dura. Indeed, ACE points are closely associated with meningeal lymphatics, which would enable the rapid drainage of CSF once it has reached the dura mater (Fig. 2c) and in fixed dura mater we observed i.c.m. tracer-positive cells around bridging veins (Extended data Fig. 6a–d). We performed intravital transcranial imaging of mice following i.c.m. tracer injection and noted that tracers followed the bridging veins toward the sinus (Fig. 2d, Supplementary video 8). We speculated that this phenomenon explained direct efflux to the dura documented in Extended data Fig. 1. Using two-photon microscopy, we confirmed that i.c.m. tracers crossed from the subarachnoid space to the dura mater at ACE points in *Prox1*-EGFP, *Dpp4*-CreER^{T2}::zsGreen, and *Cdh5*-CreER^{T2}::tdTom mice (Fig. 2e, Extended data Fig. 6e–h, Supplementary video 9–10). Notably, the regions of the dura mater with the most pronounced CSF tracer enhancement have bridging veins that project up to them from the ambient cistern and the olfactory cistern and are regions of high CSF flow [37]. Bridging veins associated with these ‘hot-spot’ regions had perivascular enhancement of i.c.m. tracers, and likely enable efflux of the majority of the CSF tracer found in the dura (Extended data Fig. 6i,j, Supplementary video 11). Indeed, we observed concentrations of ACE points at CSF efflux hot-spots, which rapidly label with CSF tracers showing a spatial association between ACE points and regions of high CSF efflux in the dura (Extended data Fig. 6 d, k–m). Because these veins are deep and project up towards the ‘hot-spots’, CSF flow under these regions could not be captured using transcranial imaging. Importantly, our results align with human MRI imaging data showing that tracers injected into the CSF accumulate around bridging veins and parasagittal regions of the dura mater [6].

It has been suggested that immune cells in the dura can influence behavior through secretion of cytokines that act in the CNS [17,18]. However, the route through which these cytokines may access the brain is unknown. We speculated that ACE points may be one such route since they create openings in the arachnoid barrier. We hypothesized that it may be possible for i.v. tracers to leak out of the fenestrated vasculature of the dura mater, and from there access the subarachnoid space. Consistent with this hypothesis, we observed the accumulation of i.v. injected tracers around subarachnoid veins on the surface of the brain (Fig. 3a,b, Extended data Fig. 7a–c). Because bridging vein endothelial cells retained their BBB properties while inside the ACE point (Extended data Fig. 5l–n), this is unlikely to represent direct leakage from the vessel lumen. Furthermore, overall BBB integrity was preserved in our mice and was not an artefact of retro-orbital i.v. injection (Extended data

Fig. 7d–h). However, we emphasize that this entry of i.v. tracers to the subarachnoid space around ACE points is limited, likely by an unfavorable hydrostatic gradient as well as phagocytic capacity of macrophages surrounding ACE points.

To directly test if ACE points permitted molecules from the dura mater to access the brain, we performed studies with transcranially applied tracers. Tracers were applied to the intact skull in a minimally invasive procedure designed to reduce the likelihood of injury-induced artefact. We selected sulfo-NHS-biotin as a low molecular weight fixable tracer for this purpose, since larger tracers did not efficiently penetrate the skull to label the dura mater. We confirmed that sulfo-NHS-biotin reached the dura when applied transcranially in this manner (Extended data Fig. 7i,j). Furthermore, we found that it reached the surface of the brain (Fig. 3c,d, Extended data Fig. 7j,k). Tracer was found within the subarachnoid space and was particularly prominent around bridging veins (Fig. 3d, Extended data Fig. 7l), and biotinylated proteins could be detected in the CSF (Fig. 3e). Kinetic studies confirmed that tracer radiated across the surface of the brain from bridging veins, but was also prominent around internal cerebral veins which extend to the dural sinuses in the transverse fissure (Extended data Fig. 7k, m–p). Importantly, we did not observe enhancement in the choroid plexus, indicating that entry to the subarachnoid space is not dependent on entry through this route (Extended data Fig. 7n–p). We suggest that ACE points facilitate exchange of molecules between the dura and subarachnoid space, enabling efflux of CSF and brain wastes as well as entry of molecules from the dura to the CSF (Fig. 3f).

Previous human MRI imaging studies have indicated that i.v. tracers reach the CSF of healthy volunteers [38], though the route through which they enter has not been established. We hypothesized that bridging veins may show similar patterns of i.v. tracer enhancement in humans. Using real-IR imaging at 3 tesla (T) MRI, which is sensitive to low concentrations of gadolinium-based contrast agent in the CSF and leptomeninges [39], to separate the gadolinium tracer-related signal in the blood and subarachnoid space, we observed rapid spreading enhancement around bridging veins in healthy participants (Fig. 4 a–d). We did not observe enhancement in the lateral ventricle, which would suggest entry through the choroid plexus (Fig. 4 b, e). Furthermore, T2*-weighted (T2*w) MRI at 7T of a healthy adult who had undergone real-IR scans confirmed that the segments of bridging veins where we observed enhancement were indeed within the subarachnoid space (Fig. 4 f). Ultrahigh resolution MRI (T2*w 0.2 mm isotropic voxels at 7T) also identified the bridging vein-parasagittal dura junction points that may correspond to putative ACE points in people (Fig. 4 g). Tracer-related enhancement was predominantly observed in older individuals. Accordingly, we observed changes to ABCs in aged mice (Extended data Fig. 8a,b, Supplementary table 3). It is also possible BBB leakage causes this phenomenon, as has been noted in the aged hippocampus [40], however we did not observe loss of the BBB marker GLUT-1 within the subarachnoid portion of bridging veins in aged mice suggesting that the BBB function of bridging veins remains intact during aging (Extended data Fig. 8 c–d). It is possible that impaired meningeal lymphatic drainage during aging leads to an overflow of fluid from the dura to the subarachnoid space [11,41]. Collectively, these data suggest that ACE point-like structures also exist in humans and likewise permit entry of molecules from the dura to the subarachnoid space. It will be important for future studies to examine the anatomical organization and molecular composition of ACE points in humans.

We hypothesized that ACE points may also permit the entry of immune cells to the subarachnoid space. Even though the dura and leptomeninges are essentially continuous due to the presence of ACE points, they have vastly different immune milieu. There are far fewer short-lived myeloid cells such as Ly-6C^{hi} monocytes and neutrophils in the leptomeninges, as well as lower numbers of adaptive immune cells such as dendritic cells, both CD4 and CD8 T cells, and B cells (Extended data Fig. 8e). In our transcriptomic dataset we identified leptomeningeal stroma, particularly in DBCs, to be enriched in chemorepellent molecules (Fig. 5a, Extended data Fig. 8f–h). Chemorepellents have predominantly been studied in the context of the developing nervous system and indeed leptomeningeal chemorepellents are likely to play important roles in cortical development. On the other hand, chemorepellents can also act on immune cells to alter their migration [42]. We identified two chemorepellents, Sema3a and Sema3d, as blunting the trafficking of monocytes toward a CCL2 gradient *in vitro* (Extended data Fig. 8i,j). We hypothesized that DBCs may regulate trafficking of immune cells through ACE points to the subarachnoid space. We used an AAV8 vector which broadly targets meningeal stromal populations, including leptomeningeal, perivascular, and dural FBs as well as DBCs (Extended data Fig. 8k,l) to deliver an shRNA against *Sema3a*. We confirmed that this reduces the expression of Sema3a in both the leptomeninges and the dura (Fig. 5b). Furthermore, in healthy mice treated with AAV8-*Sema3a*-shRNA we observed an increase in the frequency of neutrophils in the leptomeninges (Fig. 5c).

The leptomeninges is an important site of inflammation in many neurological diseases including meningitis [25,27,28], multiple sclerosis [21], and leptomeningeal metastases [22,23]. We hypothesized that changes to the leptomeningeal stroma may enhance trafficking of immune cells through ACE points in neuroinflammation. snRNA-seq of ABCs in EAE revealed enrichment of pathways related to cell migration and immunological functions (Fig. 5d, Extended data Fig. 9a, Supplementary tables 4–6), as well as patches of E-Cad staining in the spinal meninges reminiscent of ABC remodeling during development (Extended data Fig. 9b) [43]. We also observed enrichment of ECM remodeling and immunological functions in DBCs and pial and arachnoid fibroblasts suggesting concerted changes to the leptomeningeal stroma to promote the migration and retention of immune cells in EAE (Extended data Fig. 9c–f). Furthermore, we found that Sema3a in leptomeningeal lysates was reduced in EAE, suggesting that the absence of this signal may enhance trafficking of immune cells at ACE points (Fig. 5e). Accordingly, we saw enhanced numbers of neutrophils, T cells, and GR-1-positive myeloid cells around ACE points and in the leptomeninges in EAE (Fig. 5f–g, Extended data Fig. 9g–p). Furthermore, confocal imaging revealed that in EAE, immune cells could be found between the vessel wall and the ABC layer (Fig. 5h,i, Extended data Fig. 9q,r), suggesting that immune cells may indeed use these ACE points to enter the subarachnoid space.

Previous reports have indicated that interactions between laminin and Itga6 regulate the entry of leukemic blasts to the subarachnoid space, independently of trafficking at the blood-brain barrier and choroid plexus [23]. We found that laminin staining is most intense around ACE points, and its components were abundantly expressed by cells surrounding ACE points (Extended data Fig. 10a–c). We therefore hypothesized that Itga6 treatment may target migration of cells at ACE points, in the context of neuroinflammation. Indeed,

disrupting these interactions through neutralizing antibody treatment reduced the severity of EAE (Extended data Fig. 10d). We found that numbers of neutrophils and Ly-6C^{hi} monocytes were decreased in the spinal cord, despite no change or increases in the blood and spinal dura (Extended data Fig. 10e–j). We also saw reduced numbers of neutrophils around bridging veins (Extended data Fig. 10k,l). We were not able to quantify monocyte numbers around bridging veins due to the lack of specific antibodies to stain these cells in fixed specimens. We did not find significant changes to the frequency of T cells in the blood, spinal dura, spinal cord, or around bridging veins (Extended data Fig. 10m–p). Laminins-411, 421, 511, and 521 are ligands for Itga6, and the constituents for these isoforms of laminin are expressed by the cells that form ACE points (Extended data Fig. 10c) [44]. Collectively, these data suggest that laminin is an important molecule that mediates the trafficking of myeloid cells to the subarachnoid space at ACE points. Despite this, we cannot fully exclude the possibility that anti-Itga6 treatment also affects trafficking through other routes.

To define the characteristics of myeloid cell migration around bridging veins, we performed intravital two-photon imaging of bridging veins at the peak of EAE in *Ms4a3*-Cre::zsGreen mice. Here we observed immune cells migrating alongside the bridging vein (Fig. 5j, Supplementary video 12). The mean y displacement of cells was negative, indicating that cells were mainly moving away from the sinus and towards the ACE point, and there were more long (>80 μm) migration tracks around bridging veins than non-bridging vein regions (Fig. 5k–m). We confirmed that events represented crossing between the dura and subarachnoid space using *Prox1*-EGFP/*Ccr2*-RFP mice at the peak of EAE (Fig. 5n, Supplementary video 13). Collectively, these data indicate that, in addition to their role in molecular exchange, ACE points are regulated entry points for cells that can enable barrier-free trafficking of cells under neuroinflammatory conditions.

Discussion

The arachnoid mater forms an important CNS barrier, however there is increasing evidence that the CNS and dura mater are in constant communication. Little is known about how the arachnoid barrier balances communication and separation. We performed transcriptomics of the leptomeninges and generated mouse models for the selective targeting of leptomeningeal cell types. Most importantly, we identified discontinuities in the arachnoid barrier that we term ACE points, which enable direct fluid and cellular exchange between the dura mater and the subarachnoid space. Although we show evidence of both fluid and cellular passage between the dura mater and the subarachnoid space at ACE points, their relative importance compared to and relationship with, established routes remains to be determined.

Because leptomeningeal stroma, and particularly ABCs, are poorly captured in most sequencing datasets, ours is one of a handful of recent reports to provide transcriptomic insights into leptomeningeal stroma [27,31,32,45]. We anticipate that these data will be an important resource for the study of the leptomeninges. These data enabled the identification of existing mouse models and development of new ones for the visualization and targeting of different leptomeningeal layers. Along with the development and identification of mice that enable targeting of pial and perivascular fibroblasts (*Lum*-CreER^{T2}) and fibroblasts in the

choroid plexus and median eminence (*Tcf21*-CreER^{T2}), these models will furnish a growing toolkit for researchers to dissect the function of diverse fibroblast populations in the brain [32].

Beyond this, we identified regional specialization of the arachnoid mater. These openings in the arachnoid barrier around bridging veins, ACE points, span the CNS. Although we did not map them out here in totality, ACE points will likely also be present in other regions where veins cross the arachnoid, as well as the internal carotid and vertebral arteries [8]. In a limited way, ACE points make the subarachnoid space continuous with the dura mater, enabling the direct efflux of CSF to the dura mater, where it can be drained by meningeal lymphatics [1,14]. Our data refine the anatomy of the glymphatic system, whereby perivenous CSF efflux continues even outside of the brain parenchyma [4], and is also relevant as a terminal efflux step in other proposed CSF clearance pathways. As openings in the arachnoid barrier, ACE points are also likely enable the removal of macroscopic waste to the dura [46], a feature that would allow the removal of debris that would otherwise occlude the subarachnoid space. Although we did not quantify its relative importance here, it is tempting to speculate that ACE points account for a substantial portion of CSF efflux, particularly in humans where CSF tracers mainly accumulate in the parasagittal dura [6]. It has recently been suggested that arachnoid granulations enable the efflux of CSF to the dura, rather than blood, and indeed there are reports of arachnoid granulations that surround bridging veins, which may indicate that some granulations may be elaborations around ACE points [5,47,48].

Our observation of limited direct entry of peripheral molecules at ACE points indicates that fluid exchange between the subarachnoid space and dura can occur in both directions. Our work fits with previous findings of intravenous tracer enhancement in the leptomeninges of healthy mice [49]. There have been suggestions that the proximity of dural immune cells may mean they have an outsized effect on the brain, compared to those in more distant organs [17,18]. ACE points provide an anatomy that could plausibly explain how dural immune cells can shape behavior. The physiological factors that govern fluid flow at ACE points have not yet been determined, but are likely to be similar to those that govern CSF flow in the subarachnoid space [50–52], as well as oncotic, hydrostatic, and concentration gradients.

The leptomeninges are a critical site of inflammation in neurological diseases. We show that ACE points allow immune trafficking between the dura mater and the subarachnoid space in neuroinflammation. This process is not detectable in homeostasis and is regulated by molecules produced by the leptomeningeal stroma. We speculate that this makes the leptomeningeal immune repertoire narrower compared to the dura. It may be possible to bias trafficking through these routes to determine if the route of entry alters the phenotype of immune cells in disease. It is also possible that ACE points may represent a mechanism through which metastases [22–24] or pathogens enter the leptomeninges [25,26,28,29]. The presence of immune cells around ACE points likely mitigates the entry of pathogens to the subarachnoid space [26,28,53]. Unraveling the processes that govern the movement of cells and molecules through ACE points may provide novel therapeutic targets in neurological diseases.

In summary, we provide a cellular and functional description of the arachnoid barrier that constitutes a conceptual framework to understand how the arachnoid barrier enables both

separation and communication between meningeal layers. We describe a new aspect of functional anatomy at the arachnoid mater, ACE points, and propose that ACE points are critical for CNS waste clearance and for neuroimmune communication in physiology and pathology.

Methods

Mice.

All mice were housed and bred in a temperature (22 °C) and humidity-controlled (33–39 %) environment with a 12-hour light dark/cycle and provided with food and water ad libitum. No more than 5 mice were housed together per cage. Mice were bred in house, purchased from Jackson Laboratories, or Taconic Biosciences. Aged mice were provided by the National Institutes of Aging and used at >20 months of age. All mice were habituated for at least 1 week before experimentation, and used between 2 – 4 months, unless specified otherwise. All experiments and procedures were approved by the Institutional Animal Care and Use Committee at Washington University in St. Louis (Protocol number 200–043). The following strains were used: C57Bl/6J (JAX000664), *Ms4a3*-Cre (C57BL/6J-*Ms4a3*$^{em2(cre)Fgnx}$/J, JAX:036382), Ai6/LSL-zsGreen (B6.Cg-*Gt(ROSA)26Sor*$^{tm6(CAG-ZsGreen1)Hze}$/J, JAX007906), Ai9/LSL-tdTomato (B6.Cg-*Gt(ROSA)26Sor*$^{tm9(CAG-tdTomato)Hze}$/J, JAX007909), *Cdh5*-CreER^{T2} (C57BL/6-Tg(Cdh5-cre/ERT2)1Rha, Taconic 13073 [54]), *Col1a2*-CreERT (Tg(Col1a2-cre/ERT,-ALPP)7Cpd/J, JAX029235), *Prox1*-EGFP (gifted by Y.K. Hong, Division of Plastic and Reconstructive Surgery, Department of Surgery, Keck School of Medicine, University of South California, Los Angeles, CA, USA), *Cx3cr1*-EGFP (B6.129P2(Cg)-*Cx3cr1*^{tm1Litt}/J, JAX:005582), *Dpp4*-CreER^{T2} (generation described below), *Slc47a1*-CreER^{T2} (generation described below).

Generation of *Dpp4*-CreER^{T2} and *Slc47a1*-CreER^{T2} mice.

Dpp4-CreER^{T2} mice were generated through CRISPR-targeted insertion of a self-cleaving CreER^{T2}-P2A construct at the between the 5'-untranslated region (UTR) and exon 1 of the Dpp4 gene locus. This resulted in a *Dpp4*-P2A-CreER^{T2} peptide which was cleaved by the P2A self-cleaving peptide to the two mature proteins, under the control of the endogenous regulatory elements for the Dpp4 gene. *Slc47a1*-CreER^{T2} mice were generated through CRISPR-targeted insertion of a self-cleaving P2A-CreER^{T2} construct at the between of exon 16 of the *Slc47a1* gene locus (the terminal exon), and the 3'-UTR. This resulted in a CreER^{T2}-P2A-*Slc47a1* peptide that is cleaved by the P2A self-cleaving peptide to produce the two mature proteins, under the control of the endogenous regulatory elements for the *Slc47a1* gene. We screened out and removed random insertions and founder mice not expressing the transgene using Southern blot, and further validated that there was no disruption of endogenous gene expression. We maintained both mice as heterozygous, backcrossing them onto wild-type C57Bl/6J mice.

EAE.

$MOG_{35–55}$ (1 mg/mL) was emulsified in Freund's adjuvant (Sigma-Aldrich), with 2 mg/mL Mycobacterium tuberculosis (BD Biosciences) by mixing through a 3-way stopcock. For

controls, MOG was excluded, and replaced with PBS. Eight to 10-week old male mice were immunized in each flank subcutaneously with a total of 200 μL of emulsion. At day 0 and day 2, mice were injected with pertussis toxin (200 ng; i.p.). Unless specified otherwise, mice were euthanized at the peak of disease (day 16 – 17 post-immunization). For clinical scores, mice were monitored daily and scored as 0 = normal, 1 = limp tail, 2 = hindlimb weakness, 3 = hindlimb paralysis, 4 = forelimb involvement, 5 = moribund.

Neutralizing antibody treatment.

Mice were injected with isotype control (rat IgG2a-kappa; eBioscience, 144218) or anti-Itga6 neutralizing antibody (clone GoH3, eBioscience, 14–0495-85) at a dose of 1 mg/kg (i.p.) every 3 days, starting 2 days prior to EAE induction. Immunization was performed as above, and mice were scored as above for up to four weeks post immunization.

Intravenous injection.

Mice were anaesthetized by isoflurane inhalation and injected either retro-orbitally or in the tail vein with up to 100 μL of tracer solution. Mice were then allowed to recover on a heating pad for up to one hour.

Intracisterna magna injection/CSF collection.

Tracers were injected into the CSF by injection into the cisterna magna. Mice were anaesthetized with ketamine/xylazine (100/10 mg/mL) to achieve a surgical anaesthetic plane. The neck was shaved and cleaned with a solution of iodine in 70 % (v/v) ethanol. Mice were placed in a stereotactic frame, and the skin over the back of the neck was cut. The outermost nuchal muscles were cut, and the inner layer retracted to expose the cisterna magna. A 5 μL Hamilton syringe with a 33-gauge needle was used to inject 2 – 5 μL of tracer at a rate of approximately 2.5 μL/minute. For a full list of tracers used, see Supplementary Table 7. The needle was kept in the cisterna magna for an additional 2 minutes after the injection was complete. The open skin was then sutured, and mice were allowed to recover on a heating pad until tissue harvest, typically 30 – 60 minutes post injection. Alternatively, for two-photon imaging, the scalp was dissected and a headplate rapidly mounted over the region of interest with superglue. To harvest CSF, a similar approach was taken, where the cisterna magna was exposed, but instead of a needle, an empty glass microcapillary (Sutter Instrument, B100–50–10, pulled with a Sutter Instrument P-30 micropipette puller to a size of 0.5 mm in diameter) with the tip cut was used. CSF was allowed to fill the capillary until it reached the end, before it was flushed out with air and immediately stored on dry ice, before being frozen for long-term storage at −80 °C.

Transcranial biotin delivery.

To assess the distribution of molecules from the dura, freshly dissolved Pierce™ EZ-Link™ sulfo-NHS-biotin (50 mg/mL in sterile MilliQ water, Thermo Fisher Scientific) was applied. Tracers were injected into the CSF through access to the cisterna magna. Mice were anaesthetized with ketamine/xylazine (100/10 mg/mL) to achieve a surgical anaesthetic plane. The scalp was shaved and cleaned with a solution of iodine in 70 % ethanol. Mice were placed in a stereotactic frame, and the skin over the scalp was cut and retracted. The

skull was allowed to dry for 1 – 2 minutes, before 5 μL of sulfo-NHS-biotin was applied to the entire dorsal skull surface to form a droplet that did not touch the retracted skin. The mouse was kept in the stereotactic frame for an additional 5 minutes to avoid the droplet being disrupted. The scalp of the mouse was then sutured, and mice were allowed to recover on a heating pad before tissues or CSF were harvested.

Viral transduction.

For AAV8-mediated knockdown of Sema3a in the leptomeninges, 2×10^{12} GC (2 μL) of AAV8-GFP-U6-m-SEMA3A-shRNA (shAAV-271580, Vector Biolabs) or pAAV8-CAG-GFP (37825-AAV8, Addgene) were injected i.c.m. Three weeks later, mice were euthanized for tissue harvest, or EAE was induced as above.

Western blotting.

CSF samples collected from the cisterna magna of mice given transcranial biotin were thawed on ice. Samples were diluted in NuPAGE™ LDS Sample Buffer (NP0007, Thermo Fisher Scientific) and boiled at 95 °C for 5 minutes. Samples were loaded into a 15-well SDS-PAGE precast gel (4–15 % acrylamide gradient, #4561086, Bio-Rad) and electrophoresis performed in a Bio-Rad cassette. Briefly, samples were separated in the gel for 60 minutes at 100 V. Gels were then removed and western transfer to a methanol-treated PVDF membrane was performed on ice for 90 minutes at 75 V. Membranes were blocked in 5 % (w/v) BSA in tris-buffered saline supplemented with 0.1 % Tween-20 (TBS-T) for one hour at room temperature. Membranes were then probed overnight at 4 °C with streptavidin-HRP (1:1000, 554066, BD Biosciences) diluted in 1 % BSA in TBS-T. Membranes were then developed with a Pierce™ ECL Western Blotting Substrate kit (32106, Thermo Fisher Scientific) and imaged on a ChemiDoc™ MP Gel imaging system (Bio-Rad).

Quantitative real-time PCR (qPCR).

RNA was extracted using the RNeasy Mini kit (Qiagen). Briefly, tissues were placed into RLT buffer supplemented with 1 % β-mercaptoethanol (v/v; Sigma-Aldrich) and homogenized 1-mm ceramic beads in a bead beater. The sample was spun at 14, 000 x *g* for 3 minutes and the supernatant collected. The sample was diluted with 1 volume of 70 % ethanol and placed onto an RNA binding column. Samples were spun and membranes sequentially washed with RW1, RPE, and RPE buffers. RNase-free water was warmed to 70 °C and added to the membrane. Samples were then spun and the flow-through collected for cDNA synthesis. RNA was measured using a NanoDrop 2000 spectrophotometer (Thermo Fisher Scientific). Samples were normalized, and 1 μg of cDNA was made per sample. cDNA synthesis was performed using the iScript cDNA Synthesis Kit (Bio-Rad). cDNA synthesis was performed as per the manufacturer's instructions using a C1000-Touch thermocycler (Bio-Rad; with a priming step at 25 °C for 5 minutes, a reverse transcription step at 46 °C for 20 minutes, an inactivation step at 95 °C for one minute). cDNA was then used for qPCR, with 2 ng of cDNA starting material added to an equal volume of iTaq Universal SYBR Green solution with ROX (Bio-Rad). qPCR was performed in a 384-well plate with a 10 μL volume using a 7900HT Fast Real-Time PCR system (Thermo Fisher Scientific). Primer sequences are reported in Supplementary Table 8.

Tamoxifen-induced Cre recombination.

For *Cdh5*-CreER^{T2}, *Col1a2*- CreER^{T2}, *Dpp4*-CreER^{T2}, *Slc47a1*-CreER^{T2} mice, recombination was driven by the injection of taxmoxifen (1–2 mg in corn oil; i.p.) for five consecutive days. Mice were used at least 1 week after the final tamoxifen injection.

Fluorimetric measurement of i.c.m. tracers.

Mice were euthanized at the appropriate time point by a lethal dose of pentobarbital (Euthasol; 10 % v/v; i.p.) and perfused with PBS with heparin (0.2 % v/v). Tissues were harvested and rapidly transferred to ice-cold NP-40 lysis buffer on ice (Thermo Fisher Scientific, J60766-AP). Tissues were lysed by three freeze-thaw cycles, followed by mechanical dissociation using two ceramic 1 mm beads for 60 seconds in a Bead Mill 4 mini homogenizer (Thermo Fisher Scientific). Lysates were spun at 14 000 x *g* for 10 minutes at 4 °C, and the supernatant taken. A 12-point standard curve of FITC-dextran (0.00001 – 10 μg/mL by five-fold serial dilution) in NP-40 buffer was generated, and uninjected tissue homogenates were included to subtract tissue-specific autofluorescence. The standard curve, lysates, and negative controls were added to a 96-well plate and fluorescence (Ex 490, Em 520) were measured on a Synergy H1 (BioTek) plate reader running Gen5 software (v 3.1.1, BioTek). Following tissue-specific background subtraction, fluorescence readings were interpolated from the standard curve on GraphPad Prism (v. 10.0.2 (171)). Fluorescence readings were normalized to the protein abundance in the lysate, which was measured with the *DC* protein assay (Bio-Rad) at absorbance 750 nm on a Synergy H1 (BioTek) plate reader running Gen5 software (v 3.1.1, BioTek). As with fluorescence measurements a 12-point standard curve was generated (0.001 – 10 mg/mL by two-fold serial dilution) to interpolate.

Transmission electron microscopy.

Mice were euthanized by a lethal dose of pentobarbital (Euthasol; 10 % v/v; i.p.). Mice were not perfused, and brain tissue was immediately immersion fixed in 2.5 % glutaraldehyde/2 % paraformaldehyde in 0.15 M cacodylate buffer containing 2 mM CaCl2 at pH 7.4. Tissue was fixed for 3 days before being rinsed in cacodylate buffer, and 200 μm thick anatomical sections cut and stained with 1 % thiocarbohydrazide for one hour. For mice injected with HRP i.c.m., thick sections were processed as per Ben Zvi et al. [55] to develop the HRP signal. Briefly, 3–3′ diaminobenzidine (0.5 mg/mL) was developed in 0.1 M phosphate buffer with 0.03 % (v/v) hydrogen peroxide for 20 minutes at room temperature. Sections were then fixed in 2 % (w/v) osmium tetroxide with 1.5 % (w/v) potassium ferrocyanide for 1 hour at room temperature. For negative stain sections, these were additionally stained with 2 % osmium tetroxide for 1 hour at room temperature, before washing in ultrapure water. Sections were stained overnight in 1 % uranyl acetate at 4 °C, then washed again in ultrapure water before being stained for 30 minutes in lead aspartate (20 mM) at 60 °C. Sections were then dehydrated in an acetone series (50, 70, 90, 100, 100, 100 – 10 minutes per stage) and infiltrated with Durcupan resin with microwave assistance (Pelco BioWave Pro, Redding, CA). Samples were flat embedded in resin in an oven at 60 °C for 48 hours. Ultrathin sections (70 nm) were generated with a UC7 Ultramicrotome (Leica) and placed onto copper grids, and post-stained with 1 % (w/v) uranyl acetate and Reynold's lead (for negative stain

samples). Grids were then imaged on a JEOL JEM-1400 transmission electron microscope (Phillips) at 120 keV. For quantification, serial fields of leptomeninges were taken at 3000X objective magnification.

We based our electron microscopy assignments on several ultrastructural surveys of the leptomeninges [49,56–58]. We began assignment with DBCs (outer extent) since they tend to be the most readily detectable cellular structure. DBCs have distinctive morphology with extremely thin processes forming a multilayered structure (Fig. 1c, Extended data Fig. 3a,c,h). DBCs also have an electron dense cytoplasm. Based on the identification of DBCs, which were the outermost layer observed, we identified cell types based on their morphology and moving in towards the brain. There is a clear change of electron density in the cells immediately below the DBCs, with an intermediate electron density. We assigned this cell type as ABCs, and based on their monolayer structure, presence of tight junctions, and location (Fig. 1c, Extended data Fig. 3a,c,h). Immediately below ABCs, there is an extremely electron light layer of cells, which we classify as arachnoid fibroblasts (Fig. 1c, Extended data Fig. 3a,c). Arachnoid fibroblasts are notable for abundant mitochondria, and labrynthine interstitial spaces containing collagen bundles (Fig. 1c, Extended data Fig. 3a,c,h). These cells also sit above the subarachnoid space, where it is visible. Below this, at the lower extent of the subarachnoid space and in contact with the glia limitans superficialis, sit thin cells which we define as pial fibroblasts. These cells are frequently in contact with both the vasculature and macrophages. These cells also have gaps between them, as noted in other reports [59]. Macrophages are present just above pial fibroblasts and were identified based on prominent lysosomes and multivesicular bodies. Finally, the glia limitans superficialis can be readily identified through prominent intermediate filaments, and an intermediate electron density immediately above neuropil. Our assignments also agree with a more recent study in the developing leptomeninges as a recently published report using EM to examine the ultrastructure of the leptomeninges [32,43]. Images were quantified in FIJI, with cell boundaries manually traced to calculate the area of each cell type, and vesicles counted using the cell counter plugin (v 3.0.0). In Extended data Fig. 3a HRP-positive vesicle numbers were not calculated in capillary endothelial cells because the HRP tracer poorly penetrates the parenchyma.

Immunofluorescence.

Mice were euthanized by lethal injection of pentobarbital (Euthasol; 10 % v/v), followed by transcardiac perfusion of PBS with heparin (20 U/mL). Mice were then perfusion fixed with transcardiac perfusion of 10 % NBF (Thermo Fisher Scientific). Tissues were then harvested, and immersion fixed in 10 % NBF for an additional 24 hours (for skullcaps/duras) or 48 hours (for brains). Duras were then peeled from the skullcap and placed in PBS with azide (0.02 % v/v) until further use. Brains were then placed in 30 % sucrose (w/v, Sigma-Aldrich) in PBS for 48 – 72 hours, until they sank to the bottom of the tube. Brains were then embedded in optimal cutting temperature medium (Fisher Healthcare) and snap frozen over dry ice. Embedded brains were stored at −20 °C until further use. Brains were then cut to 40 μm thickness with a cytostat (Leica CM3050 S) and placed into PBS with azide (0.02 % w/v, Sigma-Aldrich) until further use. Before use, sections were washed twice in PBS and blocked in normal chicken serum in PBS (5 % v/v) for 30 – 60 minutes.

Primary antibodies, diluted in normal chicken serum (1 % v/v) in PBS with azide (0.02 % w/v) and triton (0.2 % v/v, Sigma-Aldrich), were added to sections overnight (for details see Supplementary table 9). Sections were washed twice in PBS, and secondary antibodies, diluted in normal chicken serum (1 % v/v) in PBS with azide (0.02 % w/v) and triton (0.2 % v/v, Sigma-Aldrich), were added for 3 – 4 hours at room temperature (for details see Supplementary table 9). Sections were washed twice in PBS, then placed onto slides and mounted using FluorSave™ mounting media (Millipore). In the brain, veins and arteries were distinguished by intense circumferential staining for αSMA with weaker vWF staining (arteries), or absent/weak αSMA with intense vWF staining (veins). In the dura, bridging veins were identified as large-caliber veins branching into the dural venous sinuses.

To generate leptomeninges flat mounts, the leptomeninges overlying the cerebral hemispheres were carefully microdissected with #5 superfine forceps (Dumont) under a stereomicroscope, and immediately fixed in either 10 % NBF overnight (Lyve1, CD31, E-cad), or ice-cold methanol for 20 minutes at −20 °C (Cldn11, Cldn5, Ocln). Immunostaining was performed as above, with leptomeninges flattened with #5 forceps (Dumont) prior to mounting.

Images were acquired on an VS200-S6 slide scanner (Olympus) with a 10X objective (NA 0.4). Regions of interest were identified, and high-magnification images were acquired using a Stellaris TCS SP8 confocal microscope (Lecia) using either a 20X objective (NA 0.75, Leica) or 40X objective (NA 1.30, Leica).

Images were analyzed using FIJI (v 2.14.0/1.54f), using a consistent DAPI threshold to identify tissue boundaries followed by measuring the intensity of the stain within the region of interest and the area of that stain, as a percentage of the region of interest. To test the intensity of stains in the leptomeninges in brain section, Dpp4 immunostaining was used as a mask, then the intensity and area of the other stain quantified. ACE point location for Extended data Fig. 6d was determined by manually aligning duras, registered to the confluence of sinuses. The coordinate of the inner bound of the ACE point was then taken as the middle of the vein where E-cadherin coverage ends (closest to the sinus). Line analyses of GLUT-1 and E-cadherin expression at ACE points were performed by manually placing a line with at least 200 μm before and after the ACE point on the middle of bridging veins in FIJI (Extended data Fig. 5n).

Multiplexed IHC labeling in formalin-fixed paraffin embedded tissue.

Tissue was processed as above for cryosectioning, however, instead of being placed in sucrose for cryopreservation, brains were sequentially dehydrated in 70 % ethanol (v/v in water), 90 % ethanol (v/v in water), 100 % ethanol (v/v in water). Dehydrated brains were embedded in paraffin wax for sectioning. FFPE blocks of tissue were sectioned using a rotary microtome (Leica) at 7 μm thickness and mounted onto Superfrost ™ Plus charged slides (Thermo Fisher Scientific).

For multiplexed labeling of leptomeningeal markers, staining was performed as described previously [60,61]. Briefly, sections heated at 60 °C for one hour to melt the wax, then immediately placed in xylene (2 × 30 min) to dissolve the wax. Sections were rehydrated

in an ethanol series (100 %, 100 %, 90 %, 80 % (in PBS), 70 % in water) followed by 3 washes in water. Heat-induced epitope retrieval was performed with Tris-EDTA pH 9.0 buffer (Abcam), supplemented with 0.05 % Tween-20 (Sigma-Aldrich) in an Aroma digital rice cooker. Samples were boiled for 4 minutes, then left to cool for a further 2 hours. Sections were washed in PBS, followed by permeabilization in PBS with Triton (0.1 % v/v) for 5 minutes. Sections were washed in PBS, then TrueBlack Lipofuscin Autofluorescence Quencher (Biotium), diluted in 70 % ethanol, was added to sections for one minute, then washed 3 times in water. Tissue was blocked for one hour in 10 % normal chicken serum (Gibco) in PBS, then primary antibodies, diluted appropriately in 1 % normal chicken serum in PBS, were added overnight at 4 °C in a humidity chamber (For antibody details see Supplementary table 9). Sections were washed 3 times in PBS, then fluorescently conjugated secondary antibodies and DAPI (0.1 μg/mL, Sigma-Aldrich), diluted in 1 % normal chicken serum in PBS, were added for 3 – 4 h at room temperature in a humidity chamber (For antibody details see Supplementary table 9). Sections were washed 3 times in PBS, then a coverslip was mounted with FluorSave™ (Millipore) mounting media. Images were rapidly acquired on an VS200-S6 slide scanner (Olympus) with a 10X objective (NA 0.4) to avoid mounting media from hardening. Sections were placed into PBS overnight to gently remove coverslips, followed by washing in PBS. Antibodies were stripped with NewBlot Nitro 5X Stripping buffer (Li-Cor Biosciences) for 5 minutes. Sections were washed in PBS to remove any excess stripping buffer, then antigen retrieval performed again. At this point, a subsequent round of staining could be performed. Images were co-registered to DAPI signal using the HyperstackReg plugin in the FIJI package for ImageJ software (v 2.14.0/1.54f).

Flow cytometry.

Flow cytometry was performed as described previously [15]. Briefly, mice were euthanized by lethal injection of Euthasol (10 % v/v, i.p.) followed by transcardiac perfusion of PBS with heparin (5 U/mL). Tissues were microdissected as described above in ice-cold RPMI and placed into a solution of pre-warmed RPMI supplemented with collagenase VIII (1 mg/mL, Sigma-Aldrich) and DNase I (0.5 mg/mL, Sigma-Aldrich), and FBS (2 %, Gibco) for dissociation. Prior to enzymatic dissociation, brains were chopped with scissors and triturated ten times with a P1000 pipette. Tissues were dissociated for 20 minutes (leptomeninges, dura) and 40 minutes (brains). Tissues were passed through a 70 μm cell strainer and washed through with one volume of 10 % FBS in RPMI and 1 volume of fluorescence-activated cell sorting (FACS) buffer (2 % BSA, 1 mM ethylenediamine acetic acid (EDTA)) to quench enzyme activity. Brain samples were resuspended in 3 volumes of 22 % (w/v) BSA in PBS and centrifuged at 1000 x *g* for 10 minutes. The pellet was then resuspended and transferred to a V-bottom plate (450 x *g*, 5 min). Viability staining was performed using Zombie NIR (1 in 500 in PBS, BioLegend) for 20 minutes at room temperature. Suspensions were then pelleted and resuspended in anti-CD16/32 antibody (1:100, BioLegend) diluted in FACS buffer to block Fc receptors. Cell surface stains, diluted appropriately in FACS buffer, were then added for 30 minutes on ice. For intracellular staining, suspensions were fixed and permeabilized using the Transcription Factor Fixation/ Permeabilization Kit (eBioscience) per the manufacturer's instructions. Antibodies against intracellular proteins, diluted in permeabilization buffer, were added for 30 minutes on ice. Samples were resuspended in FACS buffer and analyzed using an Aurora spectral flow

cytometer (Cytek Biosciences) running SpectroFlo software (v 2.2.0.3, Cytek). Data were analyzed with FlowJo (v. 10, BD Biosciences).

Single-nuclei RNA sequencing.

Dorsal leptomeninges were acutely harvested in ice-cold RPMI and placed into 50 μL of nuclei isolation medium (NIM; 250 mM sucrose (Sigma-Aldrich), 25 mM KCl (Sigma-Aldrich), 5 mM $MgCl_2$ (Sigma-Aldrich), Tris-HCl (10 mM, Sigma-Aldrich), protease inhibitor cocktail (Thermo Fisher Scientific), 1 U/mL recombinant RNase inhibitor (Takara), 1 mM dithiothreitol (DTT; Sigma Aldrich), 0.1 % (v/v) Triton X-100 (Sigma-Aldrich), pH 7.5). Samples were mechanically dissociated by chopping for 10 minutes, before the volume was raised to 1 mL with NIM. Leptomeninges were dounced 10 times with pestle A, and 10 times with pestle B before being mashed through a 30 μm cell strainer with a glass pestle and washed 3 times with NIM to collect any remaining nuclei. Samples were transferred to lo-bind tubes (Eppendorf) and spun at 1500 x *g* for 10 minutes, and the supernatant discarded. Nuclei were then resuspended in 1 mL of 1 % BSA with 1 U/mL recombinant RNase inhibitor and 0.2 μg/mL DAPI. Nuclei were sorted, based on positive DAPI fluorescence, with a FACsAria II (BD Biosciences) into lo-bind tubes coated with 1 % BSA with 1 U/mL recombinant RNase inhibitor. Sample loading and library construction were performed using the 10X Genomics Chromium platform and Chromium Single Cell 3' Library & Gel Bead Kit version 3 and libraries were sequenced on the Illumina NextSeq 500.

Reads were aligned to the mm10 genome using the Cellranger software pipeline provided by 10x genomics. The resulting filtered gene by cell matrices of UMI counts were read into R using the *read10xCounts* function from the Droplet Utils package. Cells were first analyzed with the *scds* package with thresholds set to remove 5% with the highest doublet score (corresponding to the expected rate of doublets with 10x sequencing), followed by manual removal of cells that had greater than 3 standard deviations from the mean of either total RNA count or unique features in both directions, or percent of mitochondrial transcripts above the mean. Expression values for the final subset were then normalized using the scran and scater packages. The resulting log2 values were transformed to the natural log scale for compatibility with the Seurat (v3) pipeline [62–64].

Filtered and normalized matrices were used as input to the Seurat pipeline and samples were then integrated with the use of *FindIntegrationAnchors* and *IntegrateData*. Expression values were scaled across each gene, the effects of sequencing depth per cell, number of unique features, and percent mitochondrial reads were regressed out. Principal Components Analysis was conducted and an elbow plot was used to select components for uniform manifold approximation and projection (UMAP) analysis and clustering. Shared Nearest Neighbor (SNN) clustering optimized with the Louvain algorithm, as implemented by the Seurat *FindClusters* function was performed before manual annotation of clusters based on expression of canonical gene markers. Initial contamination in the form of clusters with markers of high mitochondrial fraction or doublets were manually removed and the finalized subset of cells was split by sample using *SplitObject* and again normalized, integrated, scaled, underwent PCA, clustering, and annotation as described above. Statistical analysis

of cluster proportions was done via a permutation test with 1,000 instances followed by bootstrapping to produce a p-value and confidence interval.

For analysis of differentially expressed genes between conditions, each sample was filtered to include genes that had at least 4 transcripts in at least 4 cells, then the top 2000 highly variable genes were determined and included for further analysis using the SingleCellExperiment *modelGeneVar* and *getTopHVGs* functions. After filtering, limma and edgeR were used to build a model and conduct differential expression testing with the *lmFit*, *contrasts.fit*, and *eBayes* functions. Results were then filtered using a Benjamini-Hochberg adjusted p-value threshold of less than 0.05 as statistically significant. Over representation enrichment analysis with Fisher's Exact test was used to determine significantly enriched Gene Ontology (GO) terms (adj. $p < 0.05$) for the sets of significantly differentially expressed genes. For each gene set, genes were separated into up- and down-regulated and separately [65] the *enrichGO* function from the clusterProfiler package was used with a gene set size set between 10 and 500 genes and p-values adjusted using the Benjamini-Hochberg correction [66].

To evaluate potential physical cell-cell ligand-receptor interactions in an unbiased way, the RNAMagnet package [67] was utilized with Membrane, ECM, as well as Both, ligand receptor pairs queried and all vascular, stromal, and mural cell types included as anchors for *RNAMagentAnchors*. Top pair contributions were extracted via *getRNAMagnetGenes* with a threshold set to 0.01.

RNAscope.

Animals were euthanized by a lethal dose of Euthasol (10 % v/v pentobarbital) and perfused by transcardiac perfusion of PBS with heparin (50 U/mL). Brains were extracted and rapidly frozen over a 70 % ethanol slurry on dry ice. Fresh-frozen 30 μm brain sections were cut on a cryostat (Leica CM3050S) and thaw-mounted on gelatin-coated slides and kept at −80 °C until use. Sections were then fixed in 10 % neutral buffered formalin (Fisher Scientific) for 15 minutes, and multiplexed fluorescent in situ hybridization (FISH) was performed using the RNAscope multiplex v2 assay kit (ACDBio) as per the manufacturer's instructions. Sections were then dehydrated in an ethanol series (50, 70, 100, 100 ethanol, 5 minutes each) before treatment with protease I for 30 minutes at room temperature. Hybridization was performed with *Mus musculus* probes against *Cdh1* (408658-C2, ACDBio), *Cemip* (438231-C3, ACDBio), *Rspo2* (402001, ACDBio), and *Slc47a1* (513101, ACDBio) for 2 hours at 40 °C in a humidified oven. Slides were then washed in 1X RNAscope wash buffer, before sequential hybridization of Amp probes 1, 2, and 3 for 30 minutes at 40 °C, followed by washing.

Optical tissue clearing and lightsheet microscopy.

Following injection of tracers into the cisterna magna, animals were euthanized by a lethal dose of Euthasol (10 % v/v pentobarbital) and perfused by transcardiac perfusion of PBS with heparin (50 U/mL). Tissues were perfusion fixed with 10 % NBF and immersion fixed for a further 3 days in 10 % NBF. The base of the skull was removed with scissors to relieve tension on dorsal bridging veins connected to the sagittal and transverse sinuses.

Tissue was decalcified either in 15 % EDTA (w/v, Sigma-Aldrich, pH 8.0) in PBS for at least 7 days, with EDTA changed daily, or in Morse's solution (10 % w/v sodium citrate, Sigma, 20 % v/v formic acid, Sigma-Aldrich) for 1 – 2 days. Tissue clearing was then performed as per Jacob et al. [8]. Heads were then dehydrated through a methanol series (20 %, 40 %, 60 %, 80 % (in PBS), 100 %, 100 %) with at least 1 hour for the first 4 steps, and overnight for the last 2. Fresh methanol was used for each experiment. Heads were decolorized with an overnight incubation of 5 % hydrogen peroxide (v/v) in methanol. Heads were then incubated overnight in a solution of 2:1 dichloromethane:methanol, followed by an overnight incubation in 100 % dichloromethane. Heads were cleared in dibenzyl ether overnight at room temperature and transferred to ethyl cinnamate overnight for refractive index matching. Imaging was performed on a UltraMicroscope II (Miltenyi Biotec) lightsheet fluorescence microscope in ethyl cinnamate. A 2.5-μm step size was used. For brains, the same process was used, with the decalcification step omitted. Images were exported and processed with Napari software (v 0.4.17rc8). It should be noted that solvent-based clearing methods cause considerable shrinkage of the brain relative to the skull, and therefore in Extended data Fig. 6 i, the subarachnoid space is artefactually enlarged.

Stereomicroscopy of CSF efflux.

CSF flow was analyzed through the intact skull of 6 week old mice. Mice were anesthetized by ketamine/xylazine (i.p.). For measurement of i.c.m. tracer appearance in perisinus regions of the dura mater, the scalp was then dissected and the skull cleaned. For measurement of i.c.m. tracer appearance in cervical lymph nodes, the skin over the throat was dissected. For measurement of i.c.m. tracer appearance in blood, the skin over the femoral vein was dissected. For all measurements, GenTeal® Tears were applied to maintain long-term moisture in the area. Mice were then injected with Evan's blue (5 % w/v, 2 μL) for CSF efflux studies in Extended data Fig. 1, or 70 kDa FITC-dextran (25 mg/mL, 3 μL) for Extended data Fig. 1j–n, into the cisterna magna, as above. Mice were rapidly transferred to a heating pad with gauze to hold the head level. Stereomicroscopy was performed (Leica) in a darkened environment with an acquisition rate of 1 frame every 10 seconds for 60 minutes. Images were analyzed using FIJI (v 2.14.0/1.54f), drawing region of interest around the dural sinuses, cervical lymph nodes, and femoral vein. The background intensity was subtracted, and transit time was calculated by measuring the latency before tracer reached 5 % of the maximal value.

Intravital two-photon microscopy.

Skull thinning was performed up to one week prior to imaging as per Roth et al. [20]. Briefly, mice were anesthetized by i.p. injection of ketamine/xylazine. The head was shaved and sterilized by application of iodine in 70 % ethanol. A midline scalp incision was made and the skin retracted. The periosteum was mechanically removed. For two-photon imaging of bridging veins, the bridging veins were initially identified through the intact skull as large vessels which expand as they progress towards the superior sagittal sinus (Fig. 2a). In Extended data Fig. 5f,g, representative matched stereomicroscopy and two-photon imaging in *Prox1*-EGFP and *Dpp4*-CreER^{T2}::zsGreen demonstrate the generic strategy for identification of bridging veins and ACE points. In general, veins were selected in the middle of the parietal bone, as they have a flatter profile, are further away from sutures, and

tend to exit the subarachnoid space further from the sinus (Extended data Fig. 6d), making them preferable to visualize. Thinning was targeted around bifurcations in the bridging veins where visible, which often occurred just prior to the ACE point. The outer layer of compact bone and the cancellous bone layer were gently removed with a burr drill on low speed. The inner layer of compact bone was then gently thinned with a blade. The scalp was then sutured, and mice allowed to recover on a heating pad. After up to a week of recovery, mice were again anesthetized by i.p. injection of ketamine/xylazine for imaging.

For imaging of CSF flow, an i.c.m. injection was then performed, as above, and a headplate rapidly mounted onto the skull. The glue was rapidly cured, and the mouse attached to the head frame. Where relevant, intravenous dyes were given immediately prior to imaging through a retroorbital injection. A drop of GenTeal Tears gel was placed on the skull for imaging with the dipping objective and imaging was performed. Imaging was performed with a A1RHD25 MP microscope (Nikon Instruments Inc., Melville, NY) equipped with a resonant scanner. Images were acquired using Nikon Elements (v. 5.20, Nikon) using a Nikon 25X water dipping objective (NA 1.1). A Chameleon Ultra II (Coherent) laser provided excitation at 920 nm for *Prox1*-EGFP, *Dpp4*-CreER^{T2}::zsGreen, *Cx3cr1*-EGFP and wild-type mice, 850 nm for *Cdh5*-CreER^{T2}::zsGreen, and 950 nm for *Cdh5*-CreER^{T2}::tdTomato mice. For cell migration experiments images, *Ms4a3*-Cre::tdTomato, *Ms4a3*-Cre::zsGreen, and *Ccr2*-RFP/*Prox1*-EGFP. In single color reporter mice, intravenous TxRed-dextran 70 kDa or FITC-dextran 70 kDa injected to label the vasculature. For *Ms4a3* mice, 920 nm laser light was used, and 990 nm laser light was used for *Ccr2*-RFP/*Prox1*-EGFP mice.

Semaphorin 3a/3d ELISA.

Commercially available murine semaphorin-3a (EL020980MO, CusaBio) and semaphorin-3d (EL020983MO, CusaBio) assays were performed as per the manufacturers' instructions. For CSF samples, 10 μL was assayed per sample. Leptomeninges were microdissected and placed in 100 μL of PBS, before being freeze-thawed three times to lyse cells. The suspension was spun at 14 000 x *g* for 10 minutes and the supernatant taken for assay. Protein concentrations in leptomeningeal lysates were measured using the Pierce™ BCA Protein Assay Kit (Thermo Fisher Scientific). For leptomeninges, 40 μL of lysate was assayed in duplicate per sample. Quantification was performed using an 8-point standard curve, with 450 nm absorbance read from a Synergy H1 plate reader using Gen5 software.

Human participants.

Imaging and demographic data were collected from 10 healthy volunteers with institutional review board approval and after written, informed consent, as part of the National Institute of Neurological Disorders and Stroke's "Evaluation of Progression in Multiple Sclerosis by Magnetic Resonance Imaging" protocol (NCT00001248). In this protocol, participants with multiple sclerosis or its mimics, as well as healthy volunteers, undergo 3T and/or 7T MRI of the brain and/or spinal cord, with a variety of advanced research pulse sequences. Imaging data were obtained between June 2021 and October 2022. 7T images were acquired in February 2022 and March 2023 from the same healthy volunteer.

Magnetic resonance imaging.

All MRI studies were performed on the same 3T Siemens Skyra scanner equipped with a 32-channel head coil. Standard-dose gadolinium-based contrast agent (GBCA; gadobutrol, 0.1 mmol/kg) was administered during the scan. All participants had 2 scan sessions. In the first session, participants underwent pre-GBCA acquisitions including T1-weighted magnetization-prepared 2 rapid acquisition of gradient echoes (T1-MP2RAGE), T2-weighted fluid attenuated inversion recovery (T2-FLAIR), T1-weighted gradient-recalled echo (T1-GRE), T2*-weighted segmented echo-planar imaging (T2*-EPI), and 3-deminsional real-reconstruction inversion recovery (real-IR). GBCA was administered during the scan, and contrast-enhanced real-IR scans were acquired a mean of 15 minutes (standard deviation: 1 minute) after administration (early time point). In the second MRI session, approximately 4 hours after GBCA administration (mean 244, standard deviation 9 minutes), the real-IR scan was repeated (late time point). Protocol details can be found in Supplementary table 10. 7 participants had 2 sessions in the same day with single dose GBCA administration in the first session. 3 participants were scanned on 2 different days (48, 42, and 83 days between the 2 sessions) with GBCA administration in both sessions. Study participants' details can be found in Supplementary table 11.

One healthy volunteer had 2 scan sessions on a 7T whole-body research system (Magnetom, Siemens, Erlangen, Germany) equipped with a single-channel transmit and 32-channel receiver array head coil (Nova Medical, Wilmington, MA, USA). In the first session, dedicated 0.5 mm isometric navigator-guided (nav) T2*w gradient-recalled echo (GRE) of the vertex of the brain was acquired (Fig. 4f). In the second session, navT2*w GRE at 0.2 mm isotropic voxel was acquired in the same region (Fig. 4g). Parameters of the sequences are summarized in Supplementary table 10.

MRI post-processing and image evaluation.

Image registration and evaluation were done in the ITK-SNAP environment [91]. All images were registered to T1-MP2RAGE (manufacturer-provided uniform denoised image volume) for delineation of anatomical structures. Bridging veins were identified on post-GBCA T1-GRE and T2*-EPI images as hyperintense and hypointense signal (respectively) with a vascular trajectory alongside the cortical surface connecting to major cerebral venous sinuses (superior sagittal sinus, inferior sagittal sinus, transverse sinuses). Spreading paravascular enhancement on real-IR was defined as cloud-like spreading enhancement areas within the subarachnoid space following a cortical superficial vessel trajectory, with a central tubular signal loss that overlaps with the bridging veins as identified on the post-GBCA T1-GRE and T2*-EPI scans. Images were evaluated by SVO (a neurologist with 4 years of experience in neuroimaging) and DSR (a neuroradiologist with 17 years of experience) with a consensus approach. The number of vessels with spreading paravascular enhancement was documented. Paravascular enhancing areas, dura adjacent to the enhancing vessels, and lateral ventricles, on coregistered early and late post-GBCA real-IR images, were manually marked for region-of-interest (ROI) masks by SVO to document volumes of enhancing areas at both time points. To minimize the variability resulting from factors that can affect signal intensity quantification, we computed the contrast-to-noise ratio (CNR) of signal intensity (SI, arbitrary units) for normalization and compared CNR values across the

ROIs, as follows: CNR = (SI_{ROI}- SI_{NAWM})/SD_{noise}. A 20-mm-diameter spherical ROI was positioned within the frontal white matter, while 4 spherical ROIs (each with a diameter of 20 mm) were placed in the 4 quadrants of the background noise at the middle level of axial B0 field images for CNR calculations. Longitudinal CNS changes in these ROI (spreading paravascular enhancement, adjacent dura, lateral ventricles, and white matter) were documented. 7T navT2*w GRE images at 0.5 mm and 0.2 mm isometric were reconstructed using the nonuniform Fast Fourier Transform algorithm and an in-house Matlab (Mathworks, Natick, MA, USA) program. Magnitude of T2*w GRE images was calculated as the average of the magnitude images at each echo time.

Statistics and reproducibility.

Group sizes were not determined using power calculations, but rather based on similar experiments published by our group [2,15]. Group assignment was randomly performed between cages of sex and age-matched mice. All data are presented as mean ± standard error of mean, including the individual values where possible. Unless specified otherwise, N is representative of animals. All images shown are representative of at least three independent experiments repeated with similar results. All the experiments were independently replicated at least twice, except for snRNA-seq of aged and EAE leptomeninges. Data from snRNA-seq were analyzed and plotted with R software (v 4.1.0) driving RStudio (v 1.4.1717). Data were assumed to be normally distributed, but this was not formally tested. All other data were plotted and analyzed using GraphPad Prism (v 9.0). For comparisons involving two groups, an unpaired two-tailed Student’s t-test was performed. Where repeated measures were used, a two-way repeated-measures ANOVA with Tukey’s multiple comparison test was performed. For comparisons involving one factor with at least two groups, a one-way ANOVA with Tukey’s multiple comparison adjustment. comparisons involving two factors, a two-way ANOVA with Sidak’s multiple comparison adjustment.

Extended Data

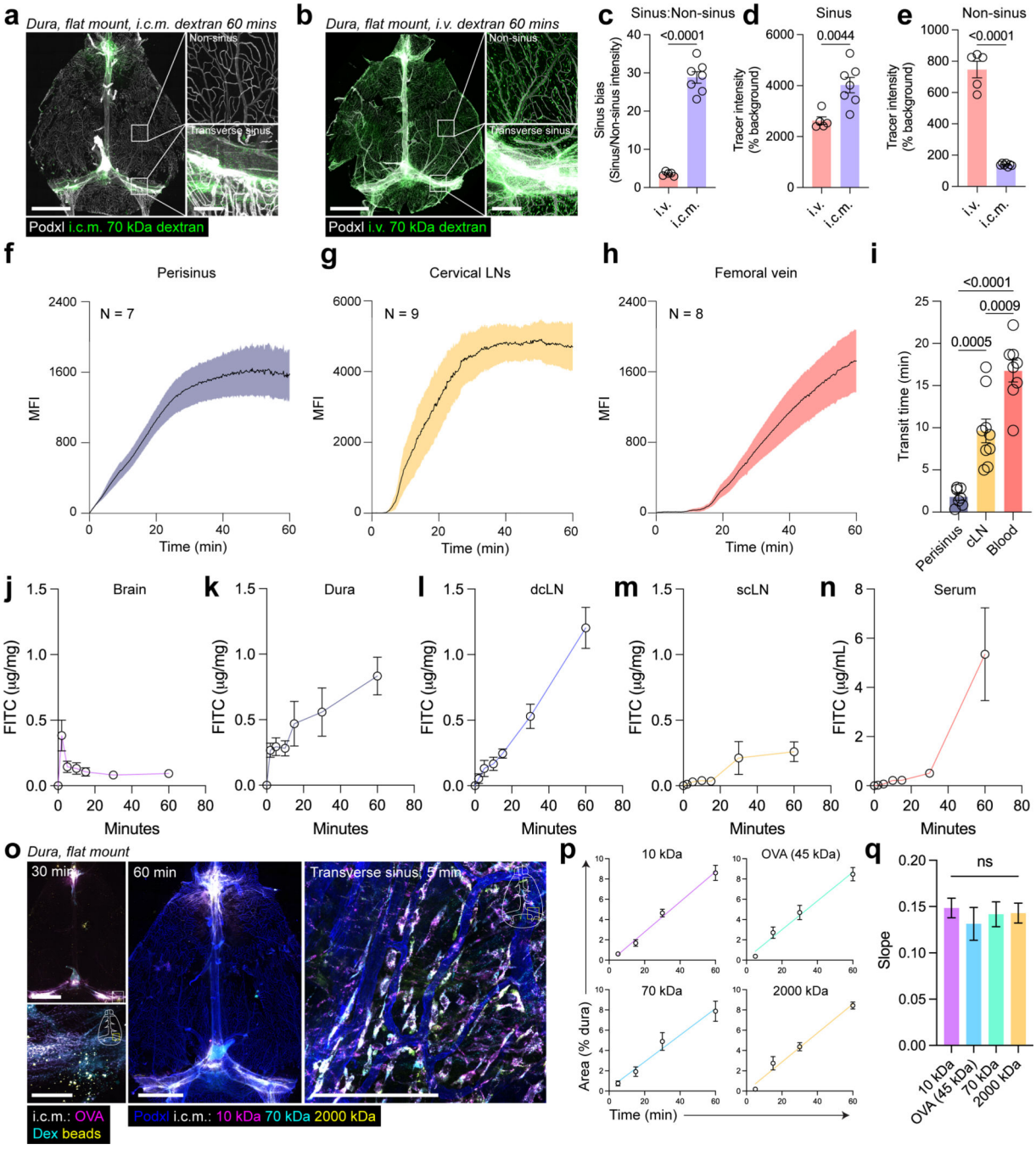

Extended data Fig. 1. Direct bulk efflux of CSF to the dura mater.

a. Flat mounted dorsal dura mater 60 minutes after i.c.m. injection of 70 kDa dextran. Scale = 2 mm, inset = 200 µm.

b. Flat mounted dorsal dura mater 60 minutes after i.v. injection of 70 kDa dextran. Scale = 2 mm, inset = 200 µm.

c. Ratio of tracer in the sinus and non-sinus regions of the dura mater 60 minutes after i.v. or i.c.m. injection. Mean ± SEM. N = 5 (i.v.), 7 (i.c.m.) animals, unpaired, two-tailed Student's t-test.

d. Tracer intensity in the sinus regions of the dura mater 60 minutes after i.v. or i.c.m. injection. Mean ± SEM. N = 5 (i.v.), 7 (i.c.m.) animals, unpaired, two-tailed Student's t-test.

e. Tracer intensity in the non-sinus regions of the dura mater 60 minutes after i.v. or i.c.m. injection. Mean ± SEM. N = 5 (i.v.), 7 (i.c.m.) animals, unpaired, two-tailed Student's t-test.

f. Evan's blue was injected i.c.m. and intravital transcranial imaging performed. Intensity of i.c.m. Evan's blue tracer in perisinus regions. Mean ± SEM. N = 7 animals.

g. Evan's blue was injected i.c.m. and intravital imaging of the cervical lymph nodes performed. Intensity of i.c.m. Evan's blue tracer in the cervical lymph nodes. Mean ± SEM. N = 9 animals.

h. Evan's blue was injected i.c.m. and intravital imaging of the femoral vein performed. Intensity of i.c.m. Evan's blue tracer in the femoral vein. Mean ± SEM. N = 8 animals.

i. Transit time (time to cross 5% max threshold) of Evan's blue signal in the perisinus regions, cervical lymph nodes, and femoral vein. Mean ± SEM. N = 7 (perisinus), 8 (femoral vein),9 (blood) animals, one-way ANOVA with Sidak's multiple comparisons test. Each point represents an animal.

j. Concentration of 70 kDa FITC dextran in the brain following i.c.m. injection. Mean ± SEM. N = 5 (0, 60 mins), 6 (2,5, 10, 15, 30 mins) animals.

k. Concentration of 70 kDa FITC dextran in the dura following i.c.m. injection. Mean ± SEM. N = 5 (0, 60 mins), 6 (2,5, 10, 15, 30 mins) animals.

l. Concentration of 70 kDa FITC dextran in the dcLN following i.c.m. injection. Mean ± SEM. N = 5 (0, 60 mins), 6 (2,5, 10, 15, 30 mins) animals.

m. Concentration of 70 kDa FITC dextran in the scLN following i.c.m. injection. Mean ± SEM. N = 5 (0, 60 mins), 6 (2,5, 10, 15, 30 mins) animals.

n. Concentration of 70 kDa FITC dextran in serum following i.c.m. injection. Mean ± SEM. N = 5 (0, 60 mins), 6 (2,5, 10, 15, 30 mins) animals.

o. Multiple molecular weight i.c.m. tracers around the transverse sinus 30, 60, and 5 minutes post injection. Scale = 2 mm, inset = 200 μm.

p. Rate of appearance of i.c.m. tracers of different molecular weight and chemical properties in the dura mater. Mean ± SEM. N = 4 (5 min), 5 (15, 30, 60 mins) animals.

q. Slope of i.c.m. tracers appearing in the dura. Mean ± SEM. N = 4 (5 min), 5 (15, 30, 60 mins) animals, one-way ANOVA with Sidak's multiple comparisons test.

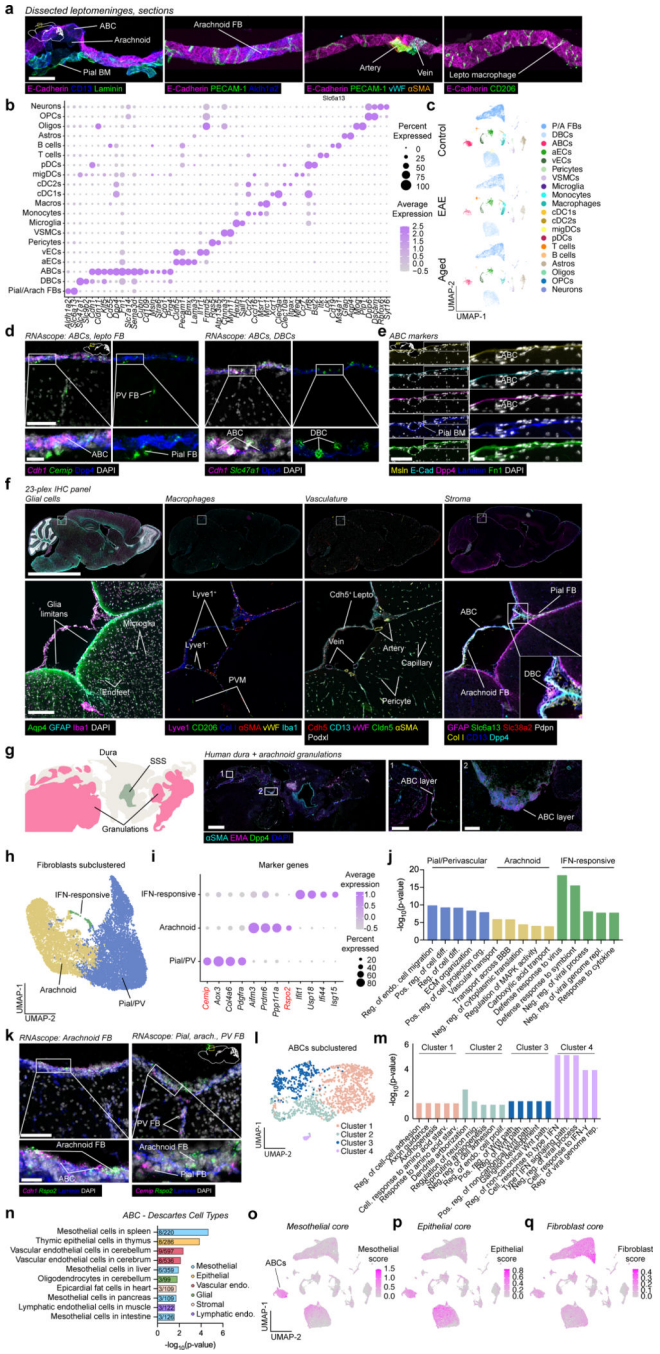

Extended data Fig. 2. Molecular mapping of the leptomeningeal stroma

a. Representative images of stromal populations in dissected leptomeninges including markers of arachnoid barrier cells (ABCs; E-Cadherin), fibroblasts (CD13, Aldh1a2), macrophages (CD206), and vasculature (αSMA, vWF, PECAM-1). Scale = 50 μm.

b. Dotplot of marker genes for cell types, with extended characterization of ABCs, colored by expression level, and scaled by proportion expressing the gene.

c. UMAPs of leptomeninges in different conditions, colored by cell type. EAE = experimental autoimmune encephalomyelitis.

d. Representative images of selected markers for ABCs (*Cdh1*), DBCs (*Slc47a1*), pial and perivascular fibroblasts (*Cemip*). Scale = 100 μm, inset = 20 μm.
e. Multiplexed IHC imaging of selected markers for ABCs (Msln, E-Cad, Dpp4, Fn1), relative to the pial basement membrane (pan-laminin). Scale = 100 μm, inset = 20 μm.
f. 23-plex IHC imaging of glial markers (Aqp4, GFAP, Iba1), macrophage markers (Lyve1, CD206, Iba1), vascular markers (Cdh5, vWF, αSMA, Cldn5, Podxl), and leptomeningeal stroma (pan: CD13, Pdpn; ABCs: Dpp4; DBCs: Slc38a2; Pial/arachnoid fibroblasts: Collagen I, Slc6a13). Scale = 4 mm, inset = 100 μm.
g. Representative images of colocalization of a novel ABC marker (Dpp4) with known ABC marker epithelial membrane antigen (EMA) in human dura-arachnoid granulation sections. Scale = 2 mm, insets = 200 μm.
h. UMAP of subclustered pial/arachnoid fibroblasts (11,092 nuclei).
i. Marker genes for pial, arachnoid, and interferon (IFN)-responsive fibroblast clusters.
j. Ontologies enriched in marker genes for each pial/arachnoid fibroblast subcluster. Enriched gene ontologies were calculated in ENRICHR using the Fisher exact test.
k. RNAscope staining of pial/perivascular fibroblasts (*Cemip*), arachnoid fibroblasts (*Rspo2*), and ABCs (*Cdh1*). FB = fibroblasts, PV = perivascular. Scale = 100 μm, inset = 200 μm.
l. UMAP of subclustered ABCs (1,871 nuclei).
m. Ontologies enriched in marker genes for each ABC subcluster. Enriched gene ontologies were calculated in ENRICHR using the Fisher exact test.
n. Enrichment of cell type-specific gene sets from the Descartes cell type atlas in ABCs, colored by the cell class. Enriched gene ontologies were calculated in ENRICHR using the Fisher exact test.
o. Leptomeningeal cell populations colored by expression score for core mesothelial genes.
p. Leptomeningeal cell populations colored by expression score for core epithelial genes.
q. Leptomeningeal cell populations colored by expression score for core fibroblast genes.

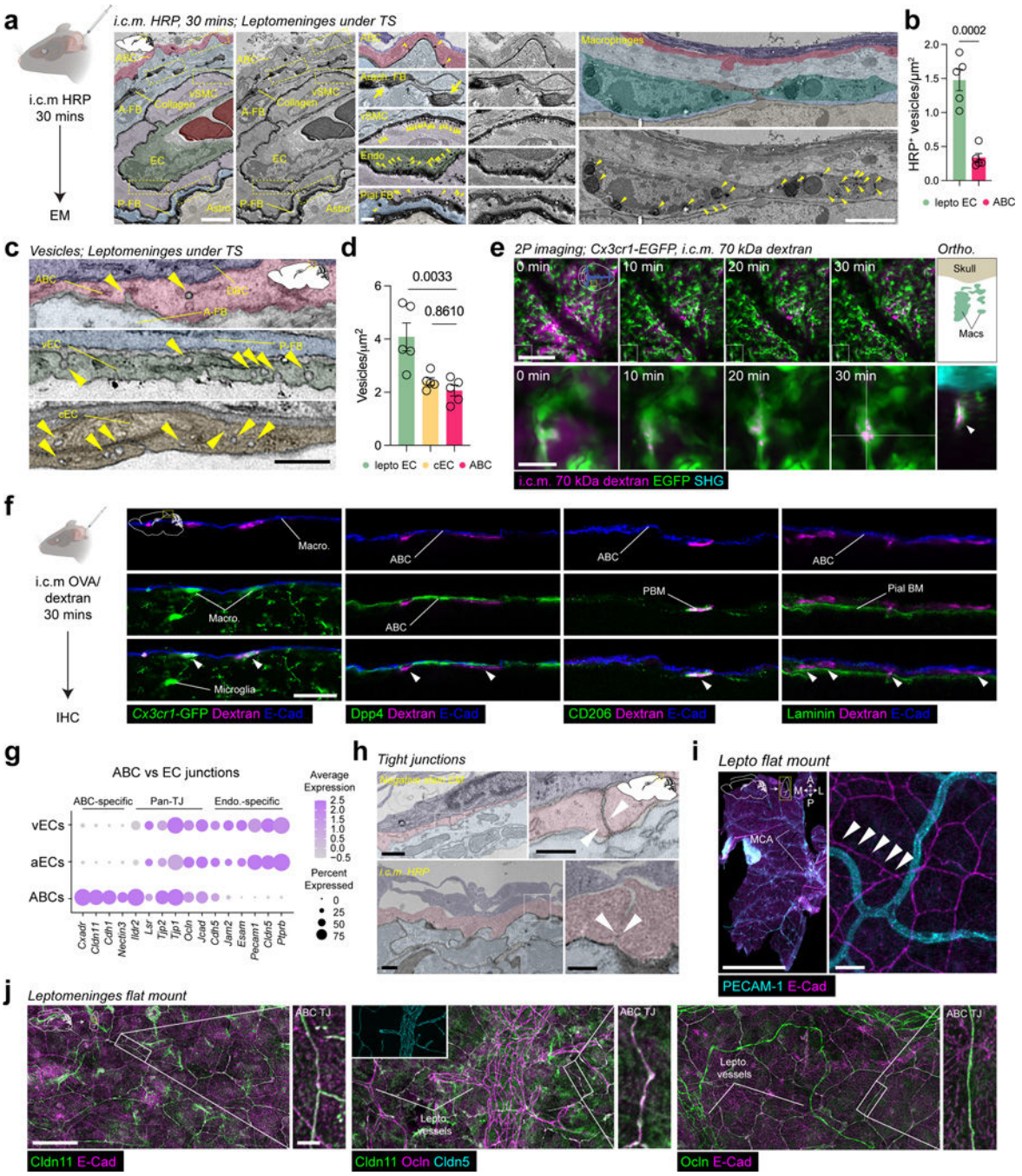

Extended data Fig. 3. Additional characterization of leptomeningeal stroma.

a. Electron micrographs of leptomeninges following i.c.m. injection of the electron microscopy (EM)-detectable tracer HRP. Representative images of the vesicle uptake by the major stromal cell types. ABC = arachnoid barrier cell. A-FB = arachnoid fibroblast. P-FB = pial fibroblast. Astro. = astrocyte. Arrowheads indicate HRP-positive vesicles, arrows indicate collagen bundles. Scale = 1 µm, inset = 200 nm.

b. Density of HRP-positive vesicles in ABCs and leptomeningeal endothelial cells (ECs, including both arterial (aECs) and venous ECs (vECs)). Mean ± SEM. N = 5 animals,

unpaired, two-tailed Student's t-test. Arrowheads indicate HRP-positive vesicles. Arrows indicate collagen bundles.

c. Negative stain EM of vesicles in ABCs, leptomeningeal endothelial cells, and capillary endothelial cells (cECs). Arrowheads indicate vesicles. Scale = 250 nm.

d. Quantification of the density of vesicles in ABCs, leptomeningeal endothelial cells (aECs and vECs pooled), and capillary endothelial cells (cECs). Mean ± SEM. N = 5 animals, one-way ANOVA with Sidak's multiple comparisons test.

e. Intravital two-photon imaging of uptake of i.c.m. tracers in *Cx3cr1*-EGFP mice. Arrowhead indicates i.v. tracer-positive macrophage. Scale = 100 μm, inset = 20 μm.

f. Experimental design and confocal images of vesicular uptake of i.c.m. 70 kDa dextran by macrophages (Cx3cr1, CD206) but not ABCs (E-Cad) in the leptomeninges of wild type and *Cx3cr1*-EGFP mice. Arrowheads indicate macrophages taking up tracer. Scale = 20 μm.

g. Dotplot of unique and shared junction components in ABCs, vECs, and aECs, colored by expression level, and scaled by proportion expressing the gene.

h. Representative images of ABC tight junctions in negative stain EM, and i.c.m. HRP injected animals. Arrowheads indicate tight junctions. Scale = 100 nm, inset = 50 nm.

i. Flat mounted leptomeninges from approximately one dorsal hemisphere, showing ubiquitous continuous E-Cad-positive junctions between ABCs. Arrowheads indicate continuous adherens junctions. Scale = 2 mm, inset = 20 μm.

j. Tight junctions formed between ABCs, including the ABC-specific junctional marker Cldn11. Colocalization with the pan-tight junction marker Ocln and ABC adherens junction marker E-Cad are shown. Scale = 25 μm, inset = 2 μm.

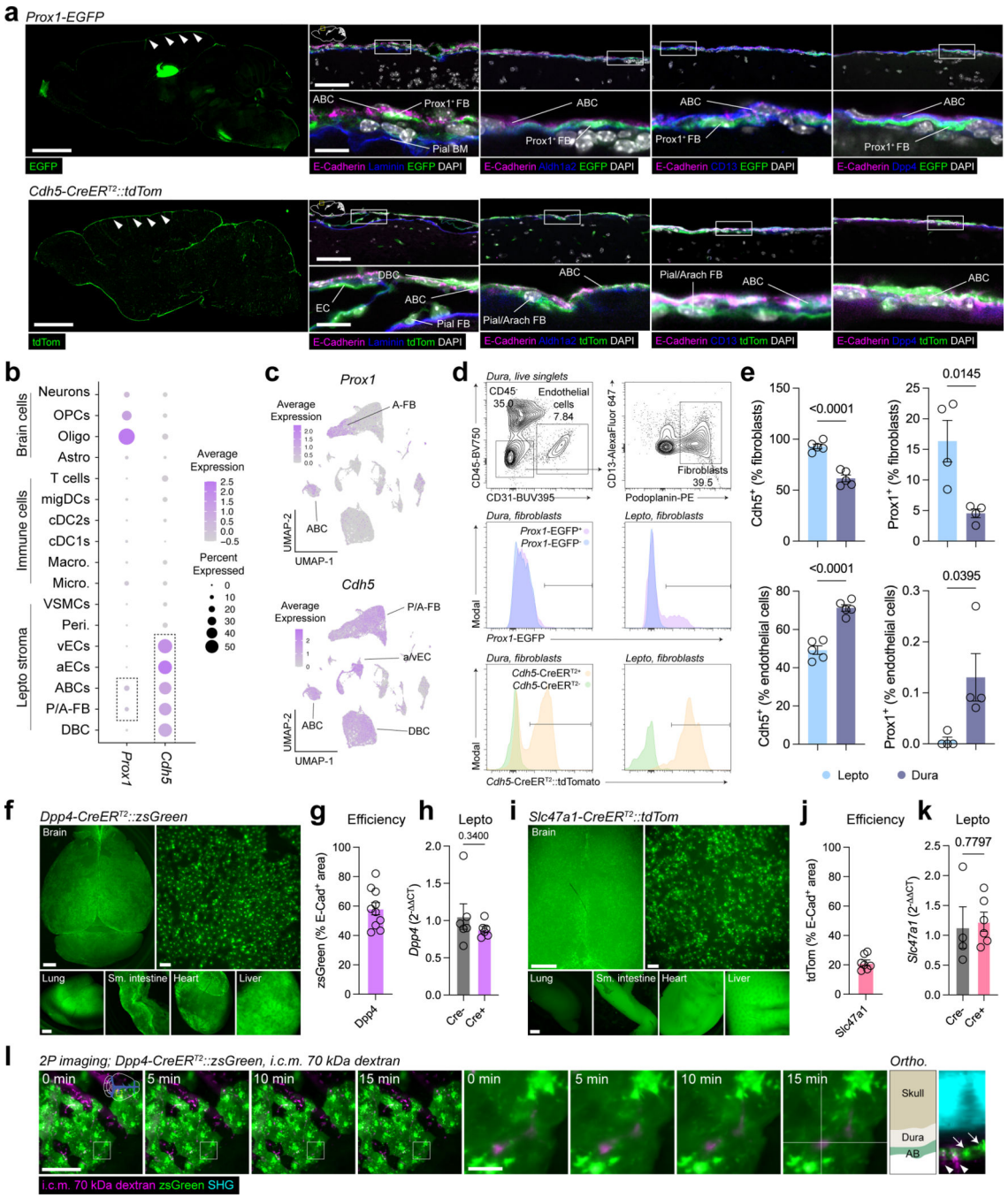

Extended data Fig. 4. Additional characterization of leptomeninges targeting mice.

a. Confocal imaging of *Prox1*-EGFP and *Cdh5*-CreER^{T2}::tdTom brains co-labeled with markers for ABCs (E-Cad, Dpp4), Fibroblasts (CD13, Aldh1a2), and the pial basement membrane (pan-laminin). Brain = 2 mm, scale = 50 μm, inset = 10 μm.

b. Dotplot of *Prox1* and *Cdh5* expression in leptomeningeal cell types, colored by expression level, and scaled by percentage expression.

c. UMAP of leptomeningeal cells, colored by expression level of *Prox1* and *Cdh5*.

d. Gating strategy and representative histograms of reporter expression in $CD45^{-}/CD31^{-}/Pdpn^{+}$ fibroblasts.

e. Efficiency of *Cdh5*-$CreER^{T2}$::tdTom and *Prox1*-EGFP for targeting fibroblasts and endothelial cells in the leptomeninges and dura. Mean ± SEM. N = 5 animals, unpaired, two-tailed Student's t-test.

f. Representative images of the brain, lung, small intestine, heart, and liver of *Dpp4*-$CreER^{T2}$::zsGreen mice. Scale = 2 mm, inset = 200 μm.

g. zsGreen coverage in the leptomeninges of *Dpp4*-$CreER^{T2}$::zsGreen. Mean ± SEM. N = 10 animals.

h. qPCR of *Dpp4* gene expression in the leptomeninges of *Dpp4*-$CreER^{T2}$ negative and heterozygous mice. Mean ± SEM. N = 6 animals, unpaired, two-tailed student's t-test.

i. Representative images of the brain, lung, small intestine, heart, and liver of *Slc47a1*-$CreER^{T2}$::tdTom mice. Scale = 2 mm, inset = 200 μm.

j. tdTomato coverage in the leptomeninges of *Slc47a1*-$CreER^{T2}$::tdTom. Mean ± SEM. N = 7 animals.

k. qPCR of *Slc47a1* gene expression in the leptomeninges of *Slc47a1*-$CreER^{T2}$ negative and heterozygous mice. Mean ± SEM. N = 4 (Cre negative) 6 (Cre positive) animals, unpaired, two-tailed student's t-test.

l. Intravital two-photon imaging of i.c.m. tracers in *Dpp4*-$CreER^{T2}$::zsGreen mice. Arrowheads indicate i.v. tracer-positive cells, arrows indicate arachnoid barrier. Scale = 100 μm, inset = 20 μm.

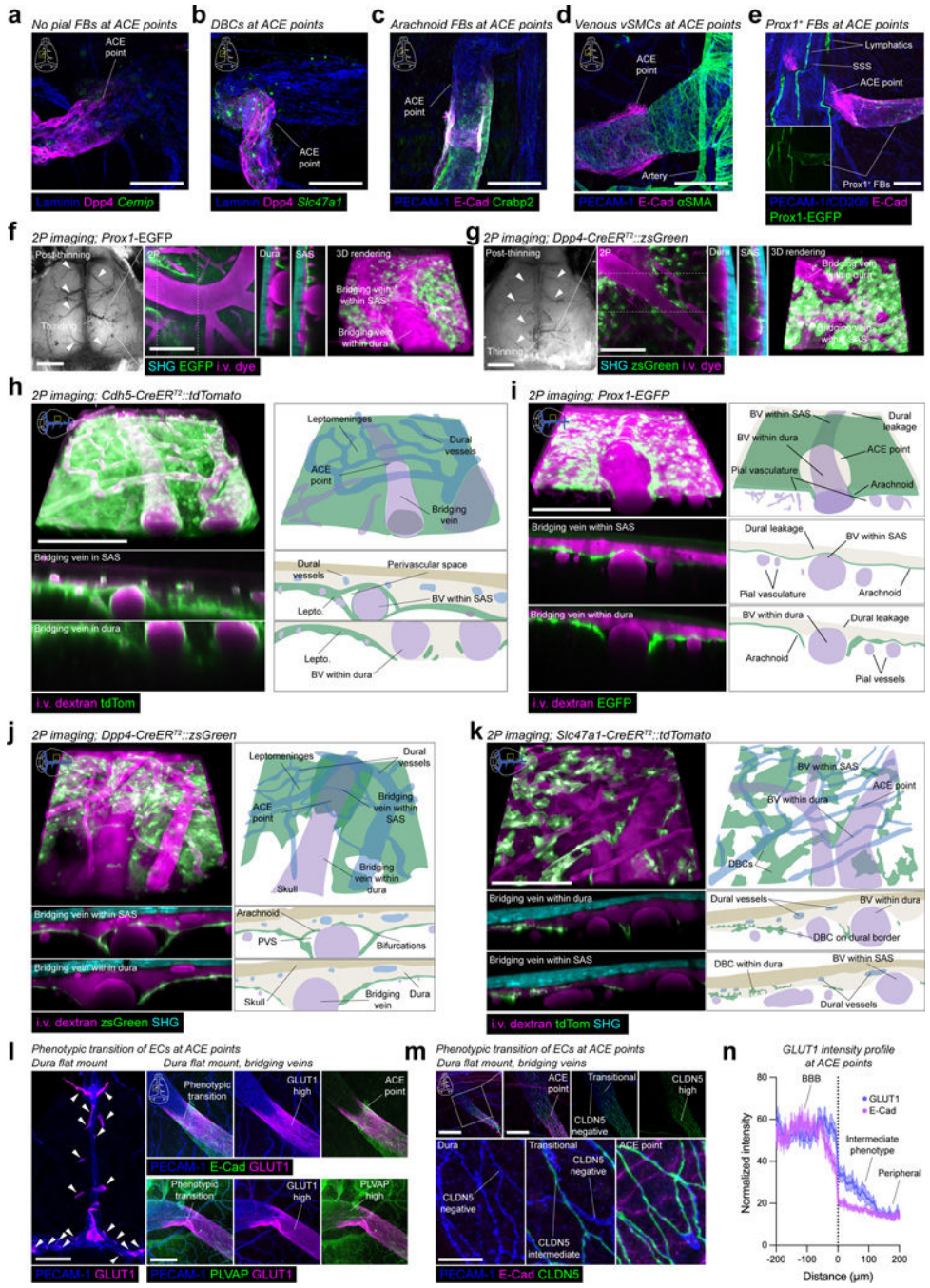

Extended data Fig. 5: Mapping the anatomy and stroma of ACE points.

a. RNAscope for the pial/perivascular fibroblast (FB) marker *Cemip* at an arachnoid cuff exit (ACE) point in a flat mounted dura mater. Scale = 200 μm.

b. RNAscope for the dural border cell (DBC) marker *Slc47a1* at an ACE point in a flat mounted dura mater. Scale = 200 μm.

c. Immunostaining for the arachnoid fibroblast marker Crabp2 at an ACE point in a flat mounted dura mater. Scale = 200 μm.

d. Immunostaining for the vascular smooth muscle marker αSMA at an ACE point in a flat mounted dura mater. Scale = 200 μm.

e. Prox1-positive fibroblasts (FBs) and lymphatic vessels around an ACE point in a *Prox1*-EGFP mouse. Scale = 200 μm.

f. Matched stereomicroscopy and two-photon intravital imaging of an ACE point around a bridging vein in a *Prox1*-EGFP mouse. Arrowheads indicate bridging veins. Scale = 2 mm, inset = 200 μm.

g. Matched stereomicroscopy and two-photon intravital imaging of an ACE point around a bridging vein in a *Dpp4*-CreER^{T2}::tdTomato mouse. Arrowheads indicate bridging veins. Scale = 2 mm, inset = 200 μm.

h. Volume rendering and diagram of an ACE point in a *Cdh5*-CreER^{T2}::tdTom mouse. Scale = 200 μm.

i. Volume rendering and diagram of an ACE point in a *Prox1*-EGFP mouse. Scale = 200 μm.

j. Volume rendering and diagram of an ACE point in *Dpp4*-CreER^{T2}::zsGreen mice. Scale = 200 μm.

k. Volume rendering and diagram of an ACE point in *Slc47a1*-CreER^{T2}::tdTom mice. Scale = 200 μm.

l. Transition of endothelial phenotype at ACE points. Staining for BBB endothelial marker GLUT-1 to peripheral endothelial marker PLVAP at ACE points. Arrowheads indicate bridging veins. Scale = 200 μm.

m. Transition of endothelial phenotype at ACE points. Staining for BBB endothelial tight junction Cldn5, and pan-endothelial junction marker PECAM-1 at an ACE point. Scale = 200 μm, inset = 100 μm, high-magnification = 10 μm.

n. Line profile of normalized GLUT1 and E-Cad intensity on bridging veins through the ACE point. N = 27 bridging veins across 5 animals, mean ± SEM of bridging veins.

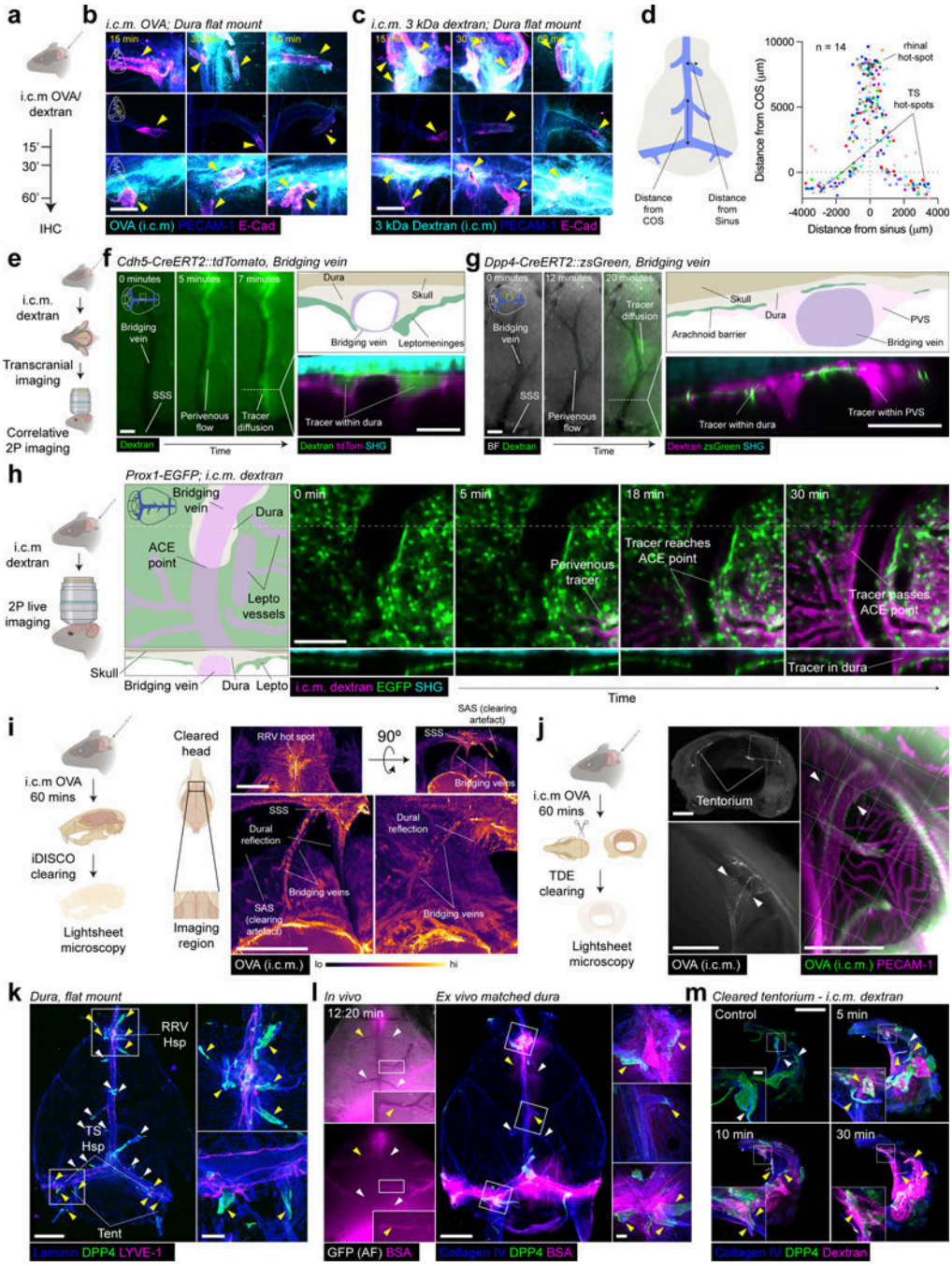

Extended data Fig. 6. Additional characterization of CSF efflux at ACE points.

a. Experimental design for examination of CSF tracer accumulation around bridging veins in the dura mater.

b. Progressive OVA accumulation around the bridging veins and in the dura mater following i.c.m. injection. Scale 200 μm.

c. Progressive dextran (3 kDa) accumulation around the bridging veins and in the dura mater following i.c.m. injection. Scale 200 μm.

d. Schematic and map of ACE points across healthy wild-type mice. N = 14 animals, each color represents the complement of ACE points from a different animal. e.

e. Experimental design for correlative transcranial and two-photon imaging of CSF efflux at ACE points.

f. Correlative stereomicroscopy and two-photon imaging of CSF tracer efflux at ACE points in *Cdh5*-CreER^{T2}::tdTom mice. Scale = 100 μm.

g. Correlative stereomicroscopy and two-photon imaging of CSF tracer efflux at ACE points in *Dpp4*-CreER^{T2}::zsGreen mice. Scale = 100 μm.

h. Two-photon intravital imaging of i.c.m. dextran flow to the dura mater through an ACE point in *Prox1*-EGFP mice. Scale = 200 μm.

i. CSF tracer accumulation around bridging veins near the rostral rhinal vein (above the olfactory bulb) in cleared heads. Scale = 1 mm.

j. CSF tracer accumulation around bridging veins in tentorial folds of the dura mater. Arrowheads indicate i.c.m.-tracer around tentorial bridging veins. Scale = 1 mm.

k. Flat mounted dura mater highlighting ACE points near the rostral rhinal vein and transverse sinus hot-spots (yellow arrowheads), as well as ACE points elsewhere in the dura mater (white arrowheads). Scale = 2 mm, inset = 200 μm.

l. Matched intravital transcranial imaging of i.c.m.-injected AlexaFluor-647-labelled bovine serum albumin (BSA) and ex vivo fixed dura mater. Note that the same bridging veins which show CSF flow (yellow arrowheads) in the intravital imaging experiment show tracer labeling while those that did not do not (white arrowheads). Scale = 2 mm, inset = 200 μm.

m. Volume renderings of cleared tentorial regions underlying the transverse sinus hot-spots following i.c.m. injection of 70 kDa dextran. Yellow arrowheads depict ACE points with tracer enhancement while white arrowheads depict those without. Scale = 2 mm, inset = 200 μm.

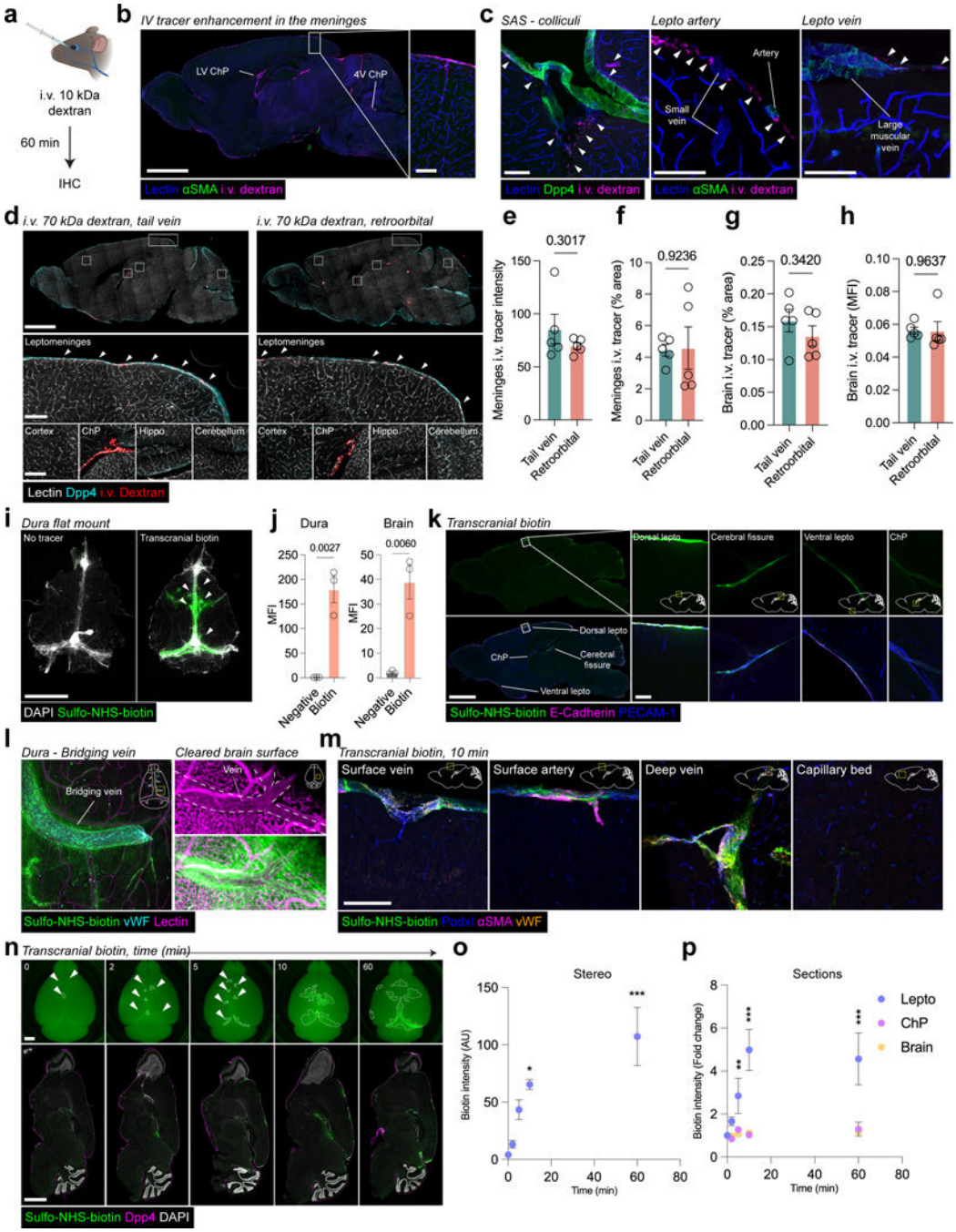

Extended data Fig. 7. Additional characterization of influx of intravenous and dural tracers at ACE points.

a. Experimental paradigm for examining the distribution of i.v. tracers on the brain surface.

b. i.v. dextran on the surface of the brain. Scale = 2 mm, inset = 200 μm.

c. i.v. dextran in the subarachnoid space and around leptomeningeal vasculature on the surface of the brain. Scale = 200 μm.

d. Images of i.v. dextran on the surface of the brain, in the cortex, choroid plexus, hippocampus, and cerebellum 60 minutes following i.v. injection through either the tail vein or retroorbital route. Scale = 2 mm, inset = 200 μm.

e. Intensity of i.v. dextran on the surface of the brain 60 minutes following i.v. injection through either the tail vein or retroorbital route. Mean ± SEM. N = 5 animals, two-tailed, unpaired Student's t-test.

f. Area of i.v. dextran on the surface of the brain 60 minutes following i.v. injection through either the tail vein or retroorbital route. Mean ± SEM. N = 5 animals, two-tailed, unpaired Student's t-test.

g. Area of i.v. dextran in the brain 60 minutes following i.v. injection through either the tail vein or retroorbital route. Mean ± SEM. N = 5 animals, two-tailed, unpaired Student's t-test.

h. Intensity of i.v. dextran in the brain 60 minutes following i.v. injection through either the tail vein or retroorbital route. Mean ± SEM. N = 5 animals, two-tailed, unpaired Student's t-test.

i. Representative images of biotin staining in flat mounted dura mater from negative control and transcranial biotin tracer duras. Arrowheads represent tracer-positive bridging veins. Scale = 4 mm.

j. Quantification of the intensity of biotin tracer in the dura mater and on the dorsal brain surface. Mean ± SEM. N = 3 animals, unpaired two-tailed Student's t-test.

k. Representative images of biotin tracer signal in the leptomeninges of sagittal brain sections. Scale = 1 mm, inset = 100 μm.

l. High-resolution image of transcranially applied biotin tracer around a bridging vein in the dorsal dura mater. Scale = 100 μm. Light sheet imaging of transcranially applied biotin and around a bridging vein in a cleared brain. Scale = 100 μm.

m. Confocal images of transcranial biotin labeling associated with surface and deep veins, surface arteries, and absent in the capillary bed ten minutes after tracer administration. Scale = 200 μm.

n. Stereomicroscopy and sagittal sections of the brain following transcranial application of sulfo-NHS-biotin. Arrowheads indicate enhancement around bridging veins. Scale = 2 mm.

o. Intensity of biotin signal in the brain surface in stereomicroscopy images. Mean ± SEM. N = 4 animals, one-way ANOVA with Dunnett's post-hoc test. 0 v 10 min, $p = 0.010$, 0 vs 60 min, $p < 0.0001$.

p. Intensity of biotin signal in the leptomeninges, cortex, and choroid plexus in sagittal sections. Mean ± SEM. N = 4 animals, two-way ANOVA with Tukey's post-hoc test. 0 v 5 min, $p = 0.0048$, 0 v 10 min, $p < 0.0001$, 0 vs 60 min, $p < 0.0001$.

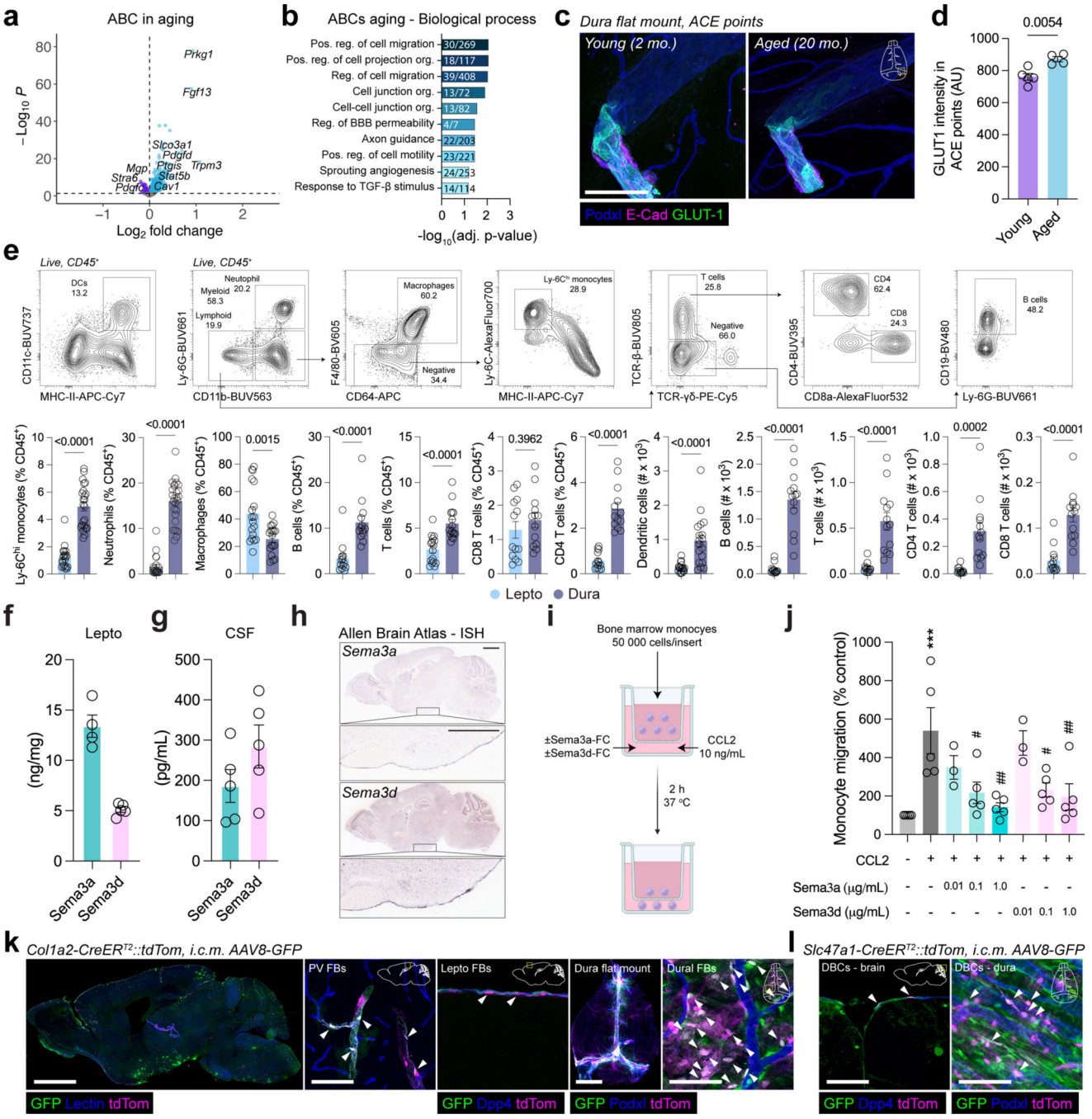

Extended data Fig. 8. Stromal Sema3a restrains myeloid infiltration to the CNS.

a. Volcano plot of differences in gene expression in arachnoid barrier cells (ABCs) in aged mice (20 month), compared to control ABCs (2 month). Benjamini-Hochberg's adjustment was used to calculate multiplicity-adjusted p-values from from unpaired two-tailed t-tests.

b. Selected significantly enriched gene ontologies in differentially expressed genes (DEGs) in control and aged ABCs. The number of DEGs as a fraction of the total gene ontology is given. Enriched gene ontologies were calculated in ENRICHR using the Fisher exact test.

c. Images of the BBB marker GLUT-1 in bridging veins in young and aged mice. Scale = 200 μm.

d. Expression of GLUT-1 within ACE points in young and aged mice. Mean ± SEM. N = 4 (aged), 5 (young), unpaired two-tailed Student's t-test.

e. Representative gating strategy for leptomeningeal and dural immune populations. Frequency of immune populations in the leptomeninges (lepto) and dura mater of healthy control mice. Mean ± SEM. N = 13 (lepto and dura B cells, cDCs, CD4, CD8), N = 15 (lepto monocytes), N = 18 (macrophages, lepto neutrophils, dura monocytes), N = 21 (dura neutrophils) animals, unpaired two-tailed Student's t-test.

f. ELISA of leptomeningeal Sema3a and Sema3d in healthy wild type mice. Mean ± SEM. N = 4 (Sema3a), 5 animals.

g. ELISA of CSF Sema3a and Sema3d in healthy wild type mice. Mean ± SEM. N = 5 animals.

h. Representative images of Sema3a and Sema3d ISH in the healthy brain taken from the Allen Brain Atlas. Scale = 1 mm, inset = 100 μm.

i. Experimental design to test the effect of semaphorins on monocyte migration *in vitro*.

j. Relative CCL2-induced monocyte transmigration in the presence of Sema3a or Sema3d. Mean ± SEM. N = 5, one-way ANOVA with Sidak's multiple comparison test. *** - $p < 0.001$ vs untreated control, # - $p < 0.05$ vs CCL2-treated, ## - $p < 0.01$ vs CCL2-treated. Each point represents cells harvested from one animal.

k. Representative images of GFP^+ perivascular, leptomeningeal, and dural fibroblasts 21 days following i.c.m. injection of AAV8-GFP (2×10^{12} GC) in *Col1a2*-$CreER^{T2}$::tdTom mice. Brain, dura = 2 mm, scale = 100 μm.

l. Representative images of GFP^+ dural border cells on the brain and dura 21 days following i.c.m. injection of AAV8-GFP (2×10^{12} GC) in Slc47a1-$CreER^{T2}$::tdTom mice. Brain, dura = 2 mm, scale = 100 μm.

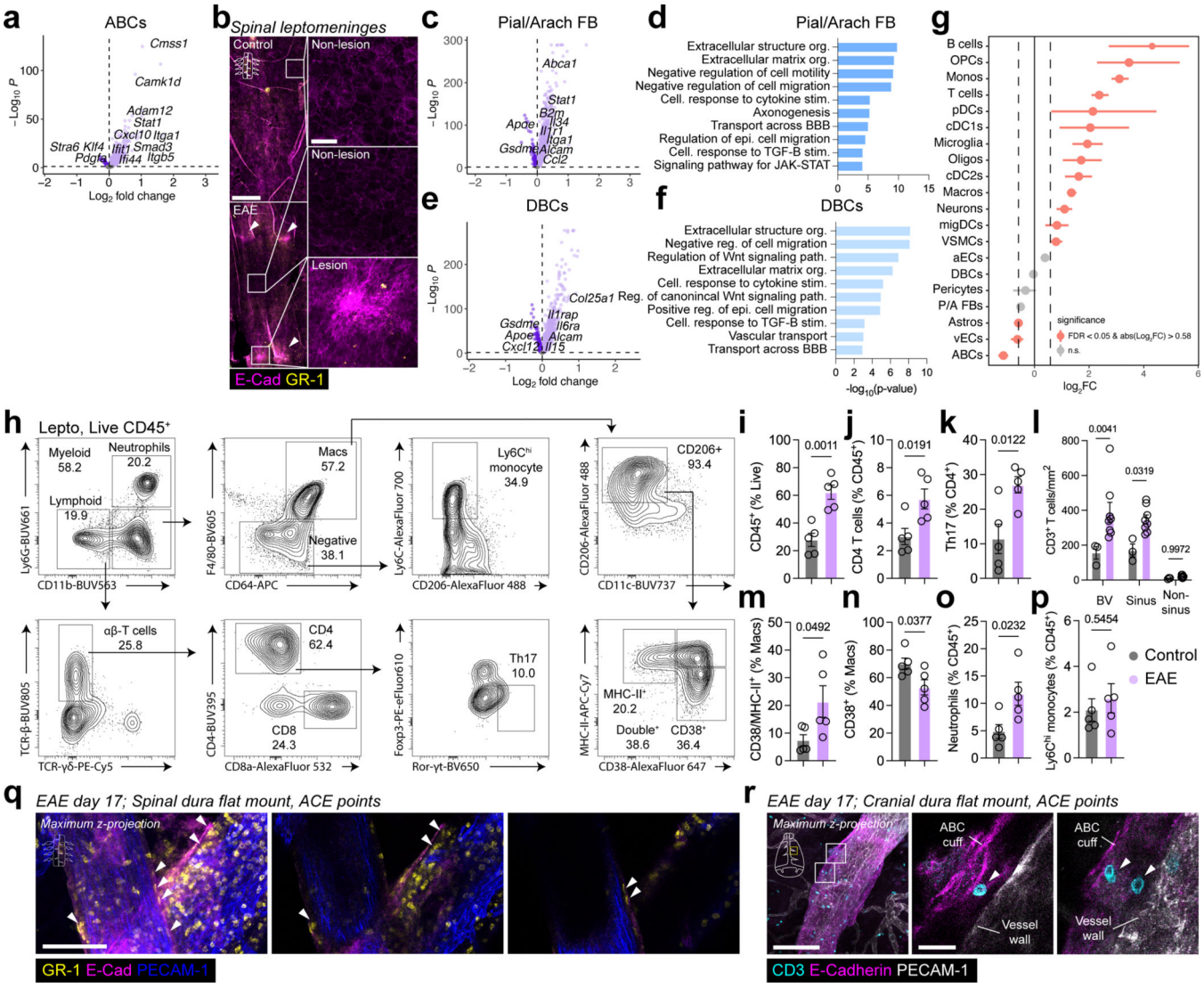

Extended data Fig. 9. Changes to stromal and immune cells in the leptomeninges during EAE and aging.

a. Volcano plot of differences in gene expression in arachnoid barrier cells (ABCs) in experimental autoimmune encephalomyelitis (EAE), compared to control ABCs. Benjamini-Hochberg's adjustment was used to calculate multiplicity-adjusted p-values from unpaired two-tailed t-tests.

b. Representative images of GR-1-positive myeloid cells within ACE points in a flat mount of the spinal cord dura mater and leptomeninges of a mouse 17 days following EAE induction. Arrowheads indicate GR-1 positive myeloid cells within the perivascular region of the ACE point. Scale = 100 μm.

c. Volcano plot of differences in gene expression in pial/arachnoid fibroblasts in EAE, compared to control pial/arachnoid fibroblasts. Benjamini-Hochberg's adjustment was used to calculate multiplicity-adjusted p-values from unpaired two-tailed t-tests.

d. Selected significantly enriched gene ontologies in differentially expressed genes (DEGs) in control and EAE pial/arachnoid fibroblasts. Enriched gene ontologies were calculated in ENRICHR using the Fisher exact test.

e. Volcano plot of differences in gene expression in dural border cells (DBCs) in EAE, compared to control DBCs. Benjamini-Hochberg's adjustment was used to calculate multiplicity-adjusted p-values from unpaired two-tailed t-tests.

f. Selected significantly enriched gene ontologies in differentially expressed genes (DEGs) in control and EAE DBCs. Enriched gene ontologies were calculated in ENRICHR using the Fisher exact test.

g. Fold changes in cell abundances in snRNA-seq from control and EAE leptomeninges, with significant differences highlighted. Mean ± 95 % CI. Data were analyzed with a permutation test of 1000 iterations to obtain the p-value and bootstrapping to obtain the confidence interval.

h. Gating strategy to examine changes to immune cell populations in EAE.

i. Frequency of $CD45^+$ immune cells, as a percentage of live cells, in control and EAE leptomeninges. Mean ± SEM. N = 5 animals, unpaired two-tailed Student's t-test.

j. Frequency of $CD4^+$ T cells, as a percentage of $CD45^+$ cells, in control and EAE leptomeninges. Mean ± SEM. N = 5 animals, unpaired two-tailed Student's t-test.

k. Frequency of Ror-γt^+ T helper 17 (T_h17), as a percentage of $CD4^+$ T cells, in control and EAE leptomeninges. Mean ± SEM. N = 5 animals, unpaired two-tailed Student's t-test.

l. Density of $CD3^+$ T cells around ACE points, sinus regions, and non-sinus regions in the dura of control and EAE mice. Mean ± SEM. N = 3 (sham control), 8 (EAE) animals, two-way ANOVA with Sidak's multiple comparison adjustment.

m. Frequency of MHC-II^+/$CD38^-$ macrophages, as a percentage of $CD206^+$ leptomeningeal macrophages, in control and EAE leptomeninges. Mean ± SEM. N = 5 animals, unpaired two-tailed Student's t-test.

n. Frequency of MHC-II^-/$CD38^+$ macrophages, as a percentage of $CD206^+$ leptomeningeal macrophages (Macs), in control and EAE leptomeninges. Mean ± SEM. N = 5 animals, unpaired two-tailed Student's t-test.

o. Frequency of neutrophils in control and EAE leptomeninges. Mean ± SEM. N = 5 animals, unpaired two-tailed Student's t-test.

p. Frequency of Ly-$6C^{hi}$ monocytes in control and EAE leptomeninges. Mean ± SEM. N = 5 animals, unpaired two-tailed Student's t-test.

q. Representative images of GR-1-positive myeloid cells within ACE points in a flat mount of the spinal cord dura mater and leptomeninges of a mouse 17 days following EAE induction. Arrowheads indicate GR-1 positive myeloid cells within the perivascular region of the ACE point. Scale = 100 μm.

r. Representative images of $CD3^+$ T cells within ACE points in a flat mount of the cranial dura mater of a mouse 17 days following EAE induction. Arrowheads indicate T cells within the perivascular region of the ACE point. Scale = 200 μm, inset = 20 μm.

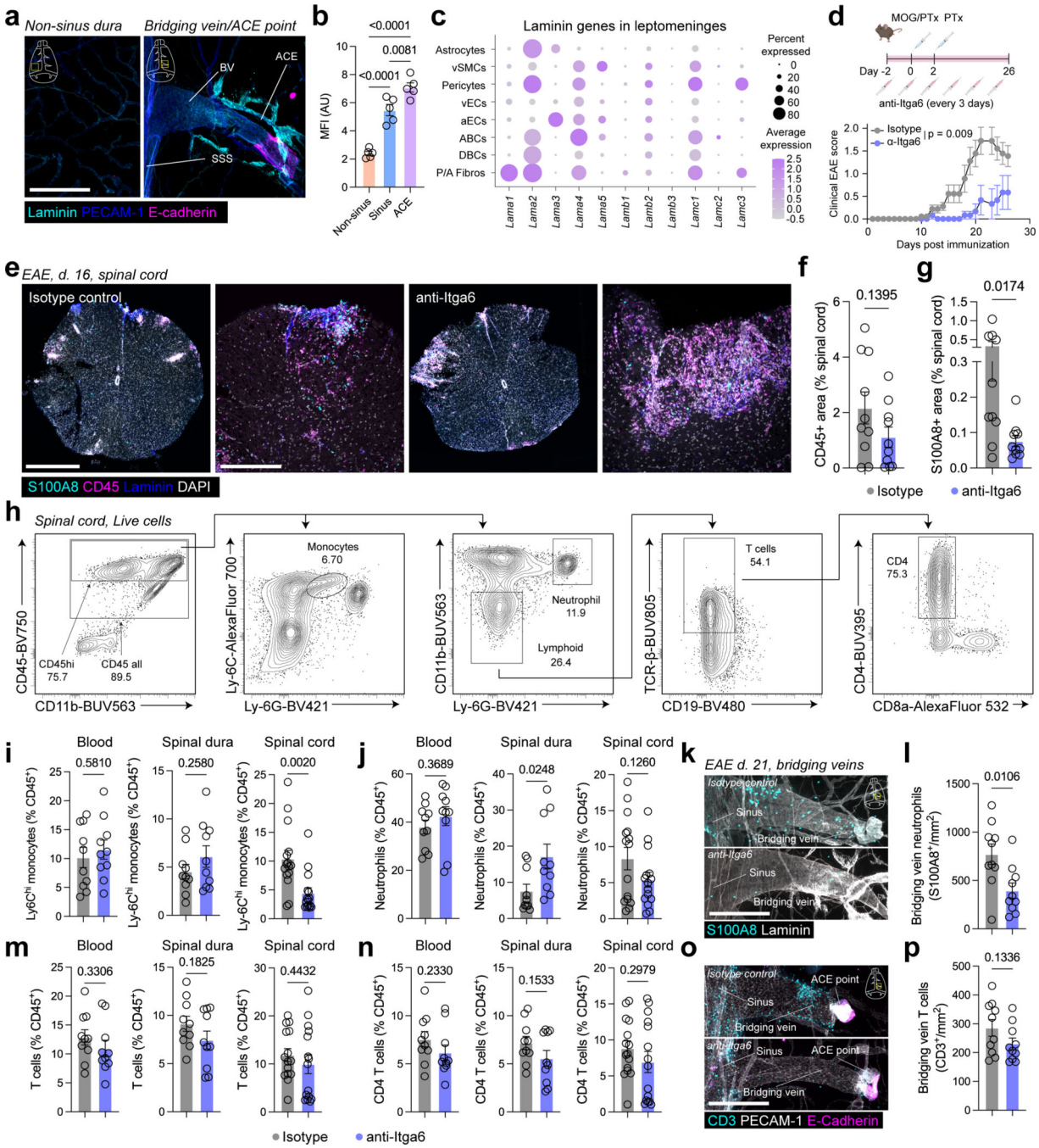

Extended data Fig. 10. Itga6-laminin interactions govern the entry of immune cells to the CNS around ACE points.

a. Laminin immunolabeling around ACE points and in non-sinus regions of the dura mater. Scale = 200 μm.

b. Quantification of laminin staining intensity in non-sinus dura, sinus, and ACE points. Mean ± SEM. N = 5 animals, one-way ANOVA with with Sidak's multiple comparison adjustment.

c. Dotplot of laminin genes in stromal populations of the leptomeninges from single nuclear RNA-sequencing, scaled by percentage of cells expressing a given gene, and its expression level.

d. Experimental paradigm for treatment of mice with anti-Itga6 antibodies in EAE and clinical scores of mice treated with isotype control, or anti-Itga6 antibody during EAE induction. Mean ± SEM. N = 6 (anti-Itga6), 9 (isotype) animals, two-way repeated measures ANOVA with Sidak's multiple comparison adjustment.

e. Representative images of CD45 and S100A8 staining in spinal cord sections in isotype control and anti-Itga6 treated mice at the peak of EAE (day 17). Scale = 1 mm, inset = 100 μm.

f. Density of $CD45^+$ area in the spinal cord of isotype control and anti-Itga6 treated mice at the peak of EAE (day 17). Mean ± SEM. N = 10 animals, two-tailed, unpaired Student's t-test.

g. Density of $S100A8^+$ neutrophils in the spinal cord of isotype control and anti-Itga6 treated mice at the peak of EAE (day 17). Mean ± SEM. N = 10 animals, two-tailed, unpaired Student's t-test.

h. Representative gating strategy for immune cells in the blood, spinal cord, and dura of EAE mice.

i. Ly-$6C^{hi}$ monocyte frequency in the blood, spinal cord, and dura of EAE mice treated with either isotype control or anti-Itga6 antibody at the peak of EAE (day 17). Mean ± SEM. N = 10 (blood, spinal dura), 15 (spinal cord) animals, two-tailed, unpaired Student's t-test.

j. Neutrophil frequency in the blood, spinal cord, and dura of EAE mice treated with either isotype control or anti-Itga6 antibody at the peak of EAE (day 17). Mean ± SEM. N = 10 (blood, spinal dura), 15 (spinal cord) animals, two-tailed, unpaired Student's t-test.

k. Staining for S100A8-positive neutrophils around bridging veins in isotype control and anti-Itga6 treated mice at the peak of EAE (day 17). Scale = 200 μm.

l. Density of neutrophils around bridging veins in isotype control and anti-Itga6 treated mice at the peak of EAE (day 17). Mean ± SEM. N = 10 animals, two-tailed, unpaired Student's t-test.

m. T cell frequency in the blood, spinal cord, and dura of EAE mice treated with either isotype control or anti-Itga6 antibody at the peak of EAE (day 17). Mean ± SEM. N = 10 (blood, spinal dura), 15 (spinal cord) animals, two-tailed, unpaired Student's t-test.

n. CD4 T cell frequency in the blood, spinal cord, and dura of EAE mice treated with either isotype control or anti-Itga6 antibody at the peak of EAE (day 17). Mean ± SEM. N = 10 (blood, spinal dura), 15 (spinal cord) animals, two-tailed, unpaired Student's t-test.

o. Staining for CD3-positive T cells around bridging veins in isotype control and anti-Itga6 treated mice at the peak of EAE (day 17). Scale = 200 μm.

p. Density of CD3-positive T cells around bridging veins in isotype control and anti-Itga6 treated mice at the peak of EAE (day 17). Mean ± SEM. N = 10 animals, two-tailed, unpaired Student's t-test.

Supplementary Material

Refer to Web version on PubMed Central for supplementary material.

Acknowledgements

We thank Elizabeth Griffin and Abena Apaw for animal care; Sean Brophy for laboratory management; and all of the members of the Kipnis lab for feedback and discussions; Gregory Strout and John Wulf in the electron microscopy core within WUCCI for sample preparation; the Flow Cytometry and Fluorescence-Activated Cell Sorting Core for sorting nuclei for sequencing; the Genome Technology Access Center for performing single-nuclei RNA-sequencing; the Washington University in St. Louis Pathology Core for paraffin embedding and sectioning. We would like to thank Dr Gwendalyn Randolph, Dr Bernd Zinselmeyer, and Alex Junidi for assistance in intravital imaging of cellular trafficking and for helpful discussions. We would like to thank Dr Xiaoxia Cui, and Jane Kouranova at the McDonnell Genome Institute for the design and generation of the *Dpp4*-CreER^{T2} and *Slc47a1*-CreER^{T2} mice. We thank Govind Bhagavatheeshwaran and the staff of the NINDS Neuroimmunology Clinic including Jeff Duyn, Peter van Gelderen, Jacco de Zwart, and Jiaen Liu and the NIMH Functional MRI Facility for assistance with human MRI collection; and all the volunteers for their contribution to the study. This work was supported by grants from the National Institutes of Health/National Institute on Aging (AG034113 and AG078106) and the Cure Alzheimer's Fund BEE consortium to J. K. This research was also partially supported by the Intramural Research Program of NINDS to D.S.R (NS003119). SVO is supported by National MS Society (Postdoctoral Fellowship Grant, FG-2208-40289).

Data and code availability

Raw data of all nuclei-cell sequencing are available on the Gene Expression Omnibus under accession numbers GSE213895. Images of *Sema3a* and *Sema3d* expression were accessed from the Allen Brain Atlas ISH browser (https://mouse.brain-map.org/).

Reference list

1. Louveau A et al. Structural and functional features of central nervous system lymphatic vessels. Nature 523, 337–341 (2015). [PubMed: 26030524]
2. Rustenhoven J et al. Functional characterization of the dural sinuses as a neuroimmune interface. Cell 184, 1000–1016.e27 (2021). [PubMed: 33508229]
3. Mastorakos P & McGavern D. The anatomy and immunology of vasculature in the central nervous system. Sci. Immunol. 4, eaav0492 (2019).
4. Iliff JJ et al. A Paravascular Pathway Facilitates CSF Flow Through the Brain Parenchyma and the Clearance of Interstitial Solutes, Including Amyloid β. Sci. Transl. Med. 4, 147ra111–147ra111 (2012).
5. Shah T et al. Arachnoid granulations are lymphatic conduits that communicate with bone marrow and dura-arachnoid stroma. J. Exp. Med. 220, e20220618 (2022).
6. Ringstad G & Eide PK. Cerebrospinal fluid tracer efflux to parasagittal dura in humans. Nat. Commun. 11, 354 (2020). [PubMed: 31953399]
7. Eide PK, Vatnehol SAS, Emblem KE & Ringstad G. Magnetic resonance imaging provides evidence of glymphatic drainage from human brain to cervical lymph nodes. Sci. Rep. 8, 7194 (2018). [PubMed: 29740121]
8. Jacob L et al. Conserved meningeal lymphatic drainage circuits in mice and humans. J. Exp. Med. 219, e20220035 (2022).
9. Spera I et al. Open pathways for cerebrospinal fluid outflow at the cribriform plate along the olfactory nerves. eBioMedicine 91, 104558 (2023).
10. Ma Q, Ineichen BV, Detmar M & Proulx ST. Outflow of cerebrospinal fluid is predominantly through lymphatic vessels and is reduced in aged mice. Nat. Commun. 8, 1434 (2017). [PubMed: 29127332]
11. Ahn JH et al. Meningeal lymphatic vessels at the skull base drain cerebrospinal fluid. Nature 572, 62–66 (2019). [PubMed: 31341278]
12. Hsu M et al. Neuroinflammation creates an immune regulatory niche at the meningeal lymphatic vasculature near the cribriform plate. Nat. Immunol. 23, 581–593 (2022). [PubMed: 35347285]
13. Absinta M et al. Human and nonhuman primate meninges harbor lymphatic vessels that can be visualized noninvasively by MRI. eLife 6, e29738 (2017).

14. Louveau A et al. CNS lymphatic drainage and neuroinflammation are regulated by meningeal lymphatic vasculature. Nat. Neurosci. 21, 1380–1391 (2018). [PubMed: 30224810]
15. Mazzitelli JA et al. Cerebrospinal fluid regulates skull bone marrow niches via direct access through dural channels. Nat. Neurosci. 25, 555–560 (2022). [PubMed: 35301477]
16. Wang Y et al. Early developing B cells undergo negative selection by central nervous system-specific antigens in the meninges. Immunity 54, 2784–2794.e6 (2021). [PubMed: 34626548]
17. Alves de Lima K et al. Meningeal γδ T cells regulate anxiety-like behavior via IL-17a signaling in neurons. Nat. Immunol. 21, 1421–1429 (2020). [PubMed: 32929273]
18. Santisteban MM et al. Meningeal interleukin-17-producing T cells mediate cognitive impairment in a mouse model of salt-sensitive hypertension. Nat. Neurosci. 1–15 (2023) doi:10.1038/s41593-023-01497-z.
19. Choi B-R, Johnson KR, Maric D & McGavern DB. Monocyte-derived IL-6 programs microglia to rebuild damaged brain vasculature. Nat. Immunol. 24, 1110–1123 (2023). [PubMed: 37248420]
20. Roth TL et al. Transcranial amelioration of inflammation and cell death after brain injury. Nature 505, 223–228 (2014). [PubMed: 24317693]
21. Magliozzi R et al. Meningeal B-cell follicles in secondary progressive multiple sclerosis associate with early onset of disease and severe cortical pathology. Brain 130, 1089–1104 (2007). [PubMed: 17438020]
22. Chi Y et al. Cancer cells deploy lipocalin-2 to collect limiting iron in leptomeningeal metastasis. Science 369, 276–282 (2020). [PubMed: 32675368]
23. Yao H et al. Leukaemia hijacks a neural mechanism to invade the central nervous system. Nature 560, 55–60 (2018). [PubMed: 30022166]
24. Remsik J et al. Leptomeningeal anti-tumor immunity follows unique signaling principles. 2023.03.17.533041 Preprint at 10.1101/2023.03.17.533041 (2023).
25. De Vlaminck K et al. Differential plasticity and fate of brain-resident and recruited macrophages during the onset and resolution of neuroinflammation. Immunity 55, 2085–2102.e9 (2022). [PubMed: 36228615]
26. Rebejac J et al. Meningeal macrophages protect against viral neuroinfection. Immunity 55, 2103–2117.e10 (2022). [PubMed: 36323311]
27. Wang J, Rattner A & Nathans J. Bacterial meningitis in the early postnatal mouse studied at single-cell resolution. eLife 12, e86130 (2023).
28. Kim Y-C et al. Immaturity of immune cells around the dural venous sinuses contributes to viral meningoencephalitis in neonates. Sci. Immunol. 8, eadg6155 (2023).
29. Pinho-Ribeiro FA et al. Bacteria hijack a meningeal neuroimmune axis to facilitate brain invasion. Nature 615, 472–481 (2023). [PubMed: 36859544]
30. Hasel P et al. Defining the molecular identity and morphology of glia limitans superficialis astrocytes in mouse and human. 2023.04.06.535893 Preprint at 10.1101/2023.04.06.535893 (2023).
31. DeSisto J et al. Single-Cell Transcriptomic Analyses of the Developing Meninges Reveal Meningeal Fibroblast Diversity and Function. Dev. Cell 54, 43–59.e4 (2020). [PubMed: 32634398]
32. Pietilä R et al. Molecular anatomy of adult mouse leptomeninges. Neuron 0, (2023).
33. Drieu A et al. Parenchymal border macrophages regulate the flow dynamics of the cerebrospinal fluid. Nature 611, 585–593 (2022). [PubMed: 36352225]
34. Park L et al. Brain Perivascular Macrophages Initiate the Neurovascular Dysfunction of Alzheimer Aβ Peptides. Circ. Res. 121, 258–269 (2017). [PubMed: 28515043]
35. Møllgård K et al. A mesothelium divides the subarachnoid space into functional compartments. Science 379, 84–88 (2023). [PubMed: 36603070]
36. Mapunda JA et al. VE-cadherin in arachnoid and pia mater cells serves as a suitable landmark for in vivo imaging of CNS immune surveillance and inflammation. Nat. Commun. 14, 5837 (2023). [PubMed: 37730744]

37. Chen X et al. Cerebral amyloid angiopathy is associated with glymphatic transport reduction and time-delayed solute drainage along the neck arteries. Nat. Aging 2, 214–223 (2022). [PubMed: 36199752]
38. Naganawa S, Nakane T, Kawai H & Taoka T. Age Dependence of Gadolinium Leakage from the Cortical Veins into the Cerebrospinal Fluid Assessed with Whole Brain 3D-real Inversion Recovery MR Imaging. Magn. Reson. Med. Sci. 18, 163–169 (2019). [PubMed: 30393275]
39. Okar SV et al. Highly Sensitive 3-Tesla Real Inversion Recovery MRI Detects Leptomeningeal Contrast Enhancement in Chronic Active Multiple Sclerosis. Invest. Radiol 10.1097/RLI.0000000000001011 doi:10.1097/RLI.0000000000001011.
40. Montagne A et al. Blood-Brain Barrier Breakdown in the Aging Human Hippocampus. Neuron 85, 296–302 (2015). [PubMed: 25611508]
41. Da Mesquita S et al. Functional aspects of meningeal lymphatics in ageing and Alzheimer's disease. Nature 560, 185–191 (2018). [PubMed: 30046111]
42. Wu JY et al. The neuronal repellent Slit inhibits leukocyte chemotaxis induced by chemotactic factors. Nature 410, 948–952 (2001). [PubMed: 11309622]
43. Derk J et al. Formation and function of the meningeal arachnoid barrier around the developing mouse brain. Dev. Cell 58, 635–644.e4 (2023). [PubMed: 36996816]
44. Schaff M et al. Integrin α6β1 Is the Main Receptor for Vascular Laminins and Plays a Role in Platelet Adhesion, Activation, and Arterial Thrombosis. Circulation (2013) doi:10.1161/CIRCULATIONAHA.112.000799.
45. Kearns NA et al. Dissecting the human leptomeninges at single-cell resolution. Nat. Commun. 14, 7036 (2023). [PubMed: 37923721]
46. Chen J et al. Meningeal lymphatics clear erythrocytes that arise from subarachnoid hemorrhage. Nat. Commun. 11, 3159 (2020). [PubMed: 32572022]
47. Upton ML & Weller RO. The morphology of cerebrospinal fluid drainage pathways in human arachnoid granulations. J. Neurosurg. 63, 867–875 (1985). [PubMed: 4056901]
48. Gailloud P et al. Anatomic relationship between arachnoid granulations in the transverse sinus and the termination of the vein of Labbé: an angiographic study. Neuroradiology 43, 139–143 (2001). [PubMed: 11326559]
49. Balin BJ, Broadwell RD, Salcman M & El-Kalliny M. Avenues for entry of peripherally administered protein to the central nervous system in mouse, rat, and squirrel monkey. J. Comp. Neurol. 251, 260–280 (1986). [PubMed: 3782501]
50. Holstein-Rønsbo S et al. Glymphatic influx and clearance are accelerated by neurovascular coupling. Nat. Neurosci. 26, 1042–1053 (2023). [PubMed: 37264158]
51. Mestre H et al. Flow of cerebrospinal fluid is driven by arterial pulsations and is reduced in hypertension. Nat. Commun. 9, 4878 (2018). [PubMed: 30451853]
52. Bojarskaite L et al. Sleep cycle-dependent vascular dynamics in male mice and the predicted effects on perivascular cerebrospinal fluid flow and solute transport. Nat. Commun. 14, 953 (2023). [PubMed: 36806170]
53. Fitzpatrick Z et al. Gut-educated IgA plasma cells defend the meningeal venous sinuses. Nature 587, 472–476 (2020). [PubMed: 33149302]
54. Wang Y et al. Ephrin-B2 controls VEGF-induced angiogenesis and lymphangiogenesis. Nature 465, 483–486 (2010). [PubMed: 20445537]
55. Ben-Zvi A et al. Mfsd2a is critical for the formation and function of the blood–brain barrier. Nature 509, 507–511 (2014). [PubMed: 24828040]
56. Schachenmayr W & Friede RL. The origin of subdural neomembranes. I. Fine structure of the dura-arachnoid interface in man. Am. J. Pathol. 92, 53–68 (1978). [PubMed: 686148]
57. Nabeshima S, Reese TS, Landis DMD & Brightman MW. Junctions in the meninges and marginal glia. J. Comp. Neurol. 164, 127–169 (1975). [PubMed: 810497]
58. Vandenabeele F, Creemers J & Lambrichts I. Ultrastructure of the human spinal arachnoid mater and dura mater. J. Anat. 189, 417–430 (1996). [PubMed: 8886963]

59. Mestre H et al. Periarteriolar spaces modulate cerebrospinal fluid transport into brain and demonstrate altered morphology in aging and Alzheimer's disease. Nat. Commun. 13, 3897 (2022). [PubMed: 35794106]

Additional references

60. Murray HC et al. Lamina-specific immunohistochemical signatures in the olfactory bulb of healthy, Alzheimer's and Parkinson's disease patients. Commun. Biol. 5, 88 (2022). [PubMed: 35075270]

61. Maric D et al. Whole-brain tissue mapping toolkit using large-scale highly multiplexed immunofluorescence imaging and deep neural networks. Nat. Commun. 12, 1550 (2021). [PubMed: 33692351]

62. Butler A, Hoffman P, Smibert P, Papalexi E & Satija R. Integrating single-cell transcriptomic data across different conditions, technologies, and species. Nat. Biotechnol. 36, 411–420 (2018). [PubMed: 29608179]

63. Lun ATL, McCarthy DJ & Marioni JC A step-by-step workflow for low-level analysis of single-cell RNA-seq data with Bioconductor. Preprint at 10.12688/f1000research.9501.2 (2016).

64. McCarthy DJ, Campbell KR, Lun ATL & Wills QF. Scater: pre-processing, quality control, normalization and visualization of single-cell RNA-seq data in R. Bioinformatics 33, 1179–1186 (2017). [PubMed: 28088763]

65. Hong G, Zhang W, Li H, Shen X & Guo Z. Separate enrichment analysis of pathways for up- and downregulated genes. J. R. Soc. Interface 11, 20130950 (2014).

66. Yu G, Wang L-G, Han Y & He Q-Y. clusterProfiler: an R Package for Comparing Biological Themes Among Gene Clusters. OMICS J. Integr. Biol. 16, 284–287 (2012).

67. Baccin C et al. Combined single-cell and spatial transcriptomics reveal the molecular, cellular and spatial bone marrow niche organization. Nat. Cell Biol. 22, 38–48 (2020). [PubMed: 31871321]

68. Yushkevich PA et al. User-guided 3D active contour segmentation of anatomical structures: Significantly improved efficiency and reliability. NeuroImage 31, 1116–1128 (2006). [PubMed: 16545965]

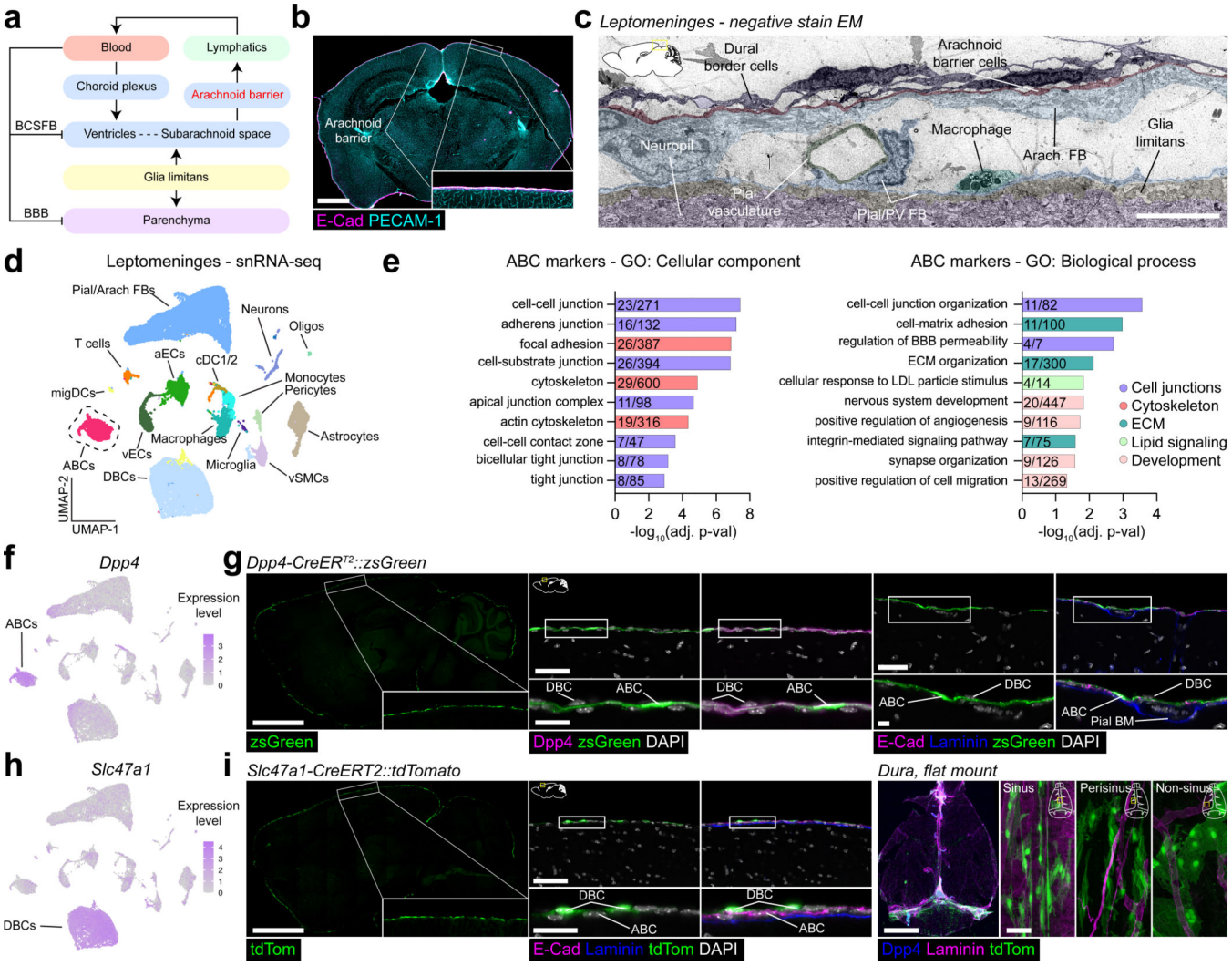

Fig. 1: Functional characterization of the arachnoid barrier.

a. Working model for fluid flow in the brain.

b. Arachnoid barrier marker E-Cadherin (E-Cad) in a coronal brain section. Scale = 1 mm.

c. Electron micrograph of the leptomeninges, highlighting the different cell types present. Scale = 5 μm.

d. Sequencing of leptomeningeal nuclei, taken from healthy mice (N = 3 independent sequencing runs with nuclei pooled from N = 5 mice), EAE mice (day 16 - peak, N = 1 with nuclei pooled from N = 5 mice), and aged mice (18–20 months old, N = 1 with nuclei pooled from N = 5 mice). UMAP of nuclei (31,346 nuclei) from all conditions, colored by cell type, containing 1871 ABC nuclei. ABC = arachnoid barrier cell. aEC = arterial endothelial cell. cDC = conventional dendritic cell. migDC = migratory dendritic cell. DBC = dural border cell. vSMC = vascular smooth muscle cell. vEC = venous endothelial cell.

e. Selected significantly enriched cellular component and biological process gene ontologies in marker genes for ABCs. The fraction of marker genes of the total gene ontology is given. Ontologies are colored by related processes. Enriched gene ontologies were calculated in ENRICHR using the Fisher exact test.

f. UMAP of leptomeningeal populations colored by *Dpp4* expression.
g. Confocal imaging of *Dpp4*-CreER^{T2}::zsGreen brains co-labeled with markers for ABCs (E-Cad, Dpp4), and the pial basement membrane (pan-laminin). Brain = 2 mm, scale = 50 um, inset = 10 μm.
h. UMAP of leptomeningeal populations colored by *Slc47a1* expression.
i. Confocal imaging of *Slc47a1*-CreER^{T2}::tdTom brains co-labeled with markers for ABCs (E-Cad), and the pial basement membrane (pan-laminin). *Slc47a1*-CreER^{T2}::zsGreen dura flat mount. Brain, dura = 2 mm, scale = 50 μm, inset = 10 μm.

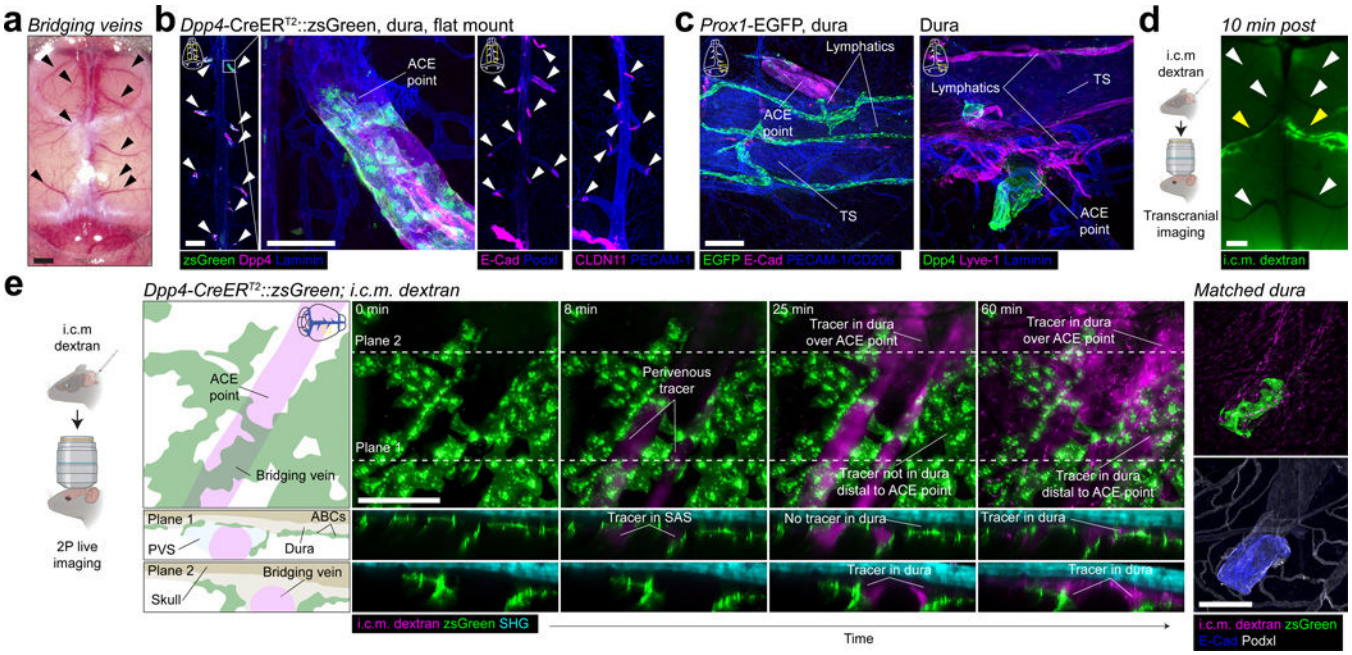

Fig. 2. Perivenous discontinuities in the arachnoid barrier allow CSF efflux to the dura mater.

a. Macroscopic image of dorsal bridging veins, also known as cerebral veins, draining into the superior sagittal sinus. Arrowheads indicate bridging veins. Scale = 1 mm.

b. Cuffs of ABCs (labeled with Dpp4) around bridging veins in *Dpp4*-CreER^{T2}::zsGreen mice, and wild-type mice (labeled with E-Cad and Cldn11). Arrowheads indicate bridging veins. Scale = 500 μm, inset = 100 μm.

c. Lymphatic vessels associated with to ACE points in the dura mater of *Prox1*-EGFP mice and wild-type mice. Scale = 200 μm.

d. Intravital transcranial imaging of i.c.m. dextran flow to the perivascular spaces of bridging veins (arrowheads are bridging veins, and are colored yellow for veins receiving tracer). Scale = 1 mm.

e. Two-photon intravital imaging of i.c.m. dextran flow to the dura mater through an ACE point in *Dpp4*-CreER^{T2}::zsGreen mice. Scale = 200 μm. Matched flat mounted dura demonstrating i.c.m. tracer around the same bridging vein. Scale = 200 μm.

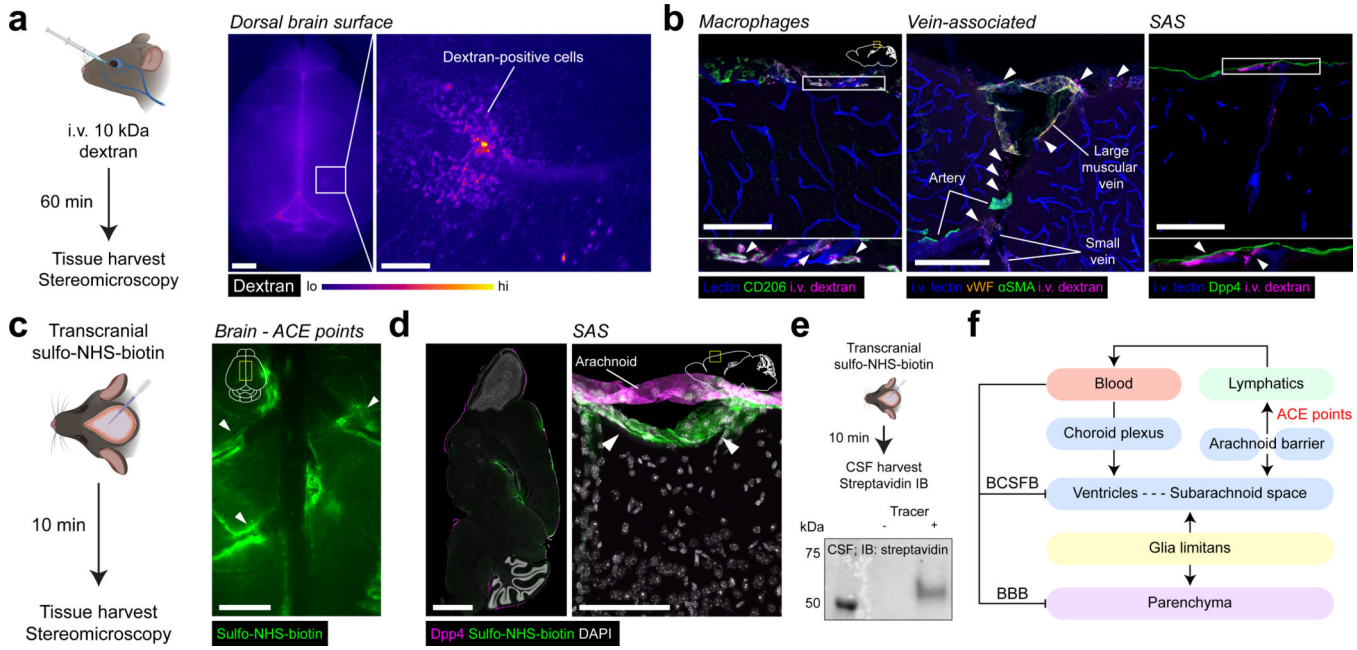

Fig. 3. ACE points allow dural molecules to enter the subarachnoid space.

a. Experimental design for detecting i.v.-injected 10 kDa dextran in the brain. Stereomicroscopy of the dorsal brain surface 60 minutes after i.v. dextran injection. Scale = 2 mm, inset = 200 μm.

b. Representative images of i.v. tracer around large leptomeningeal veins and in macrophages within the subarachnoid space. Arrowheads indicate i.v. tracer-positive cells. SAS = subarachnoid space. Scale = 200 μm.

c. Stereomicroscopy of the dorsal brain surface 10 minutes after transcranial application of sulfo-NHS-biotin. Arrowheads indicate tracer positive regions around bridging veins. Scale = 1 mm.

d. Transcranial biotin labeling in the subarachnoid space 10 minutes after after transcranial application of sulfo-NHS-biotin. Arrowheads represent tracer within the subarachnoid space. Scale = 2 mm, inset = 100 μm.

e. Experimental design and western blot for biotinylated proteins in the CSF 10 minutes after after transcranial application of sulfo-NHS-biotin.

f. Working model for fluid flow in the brain, with the addition of ACE points.

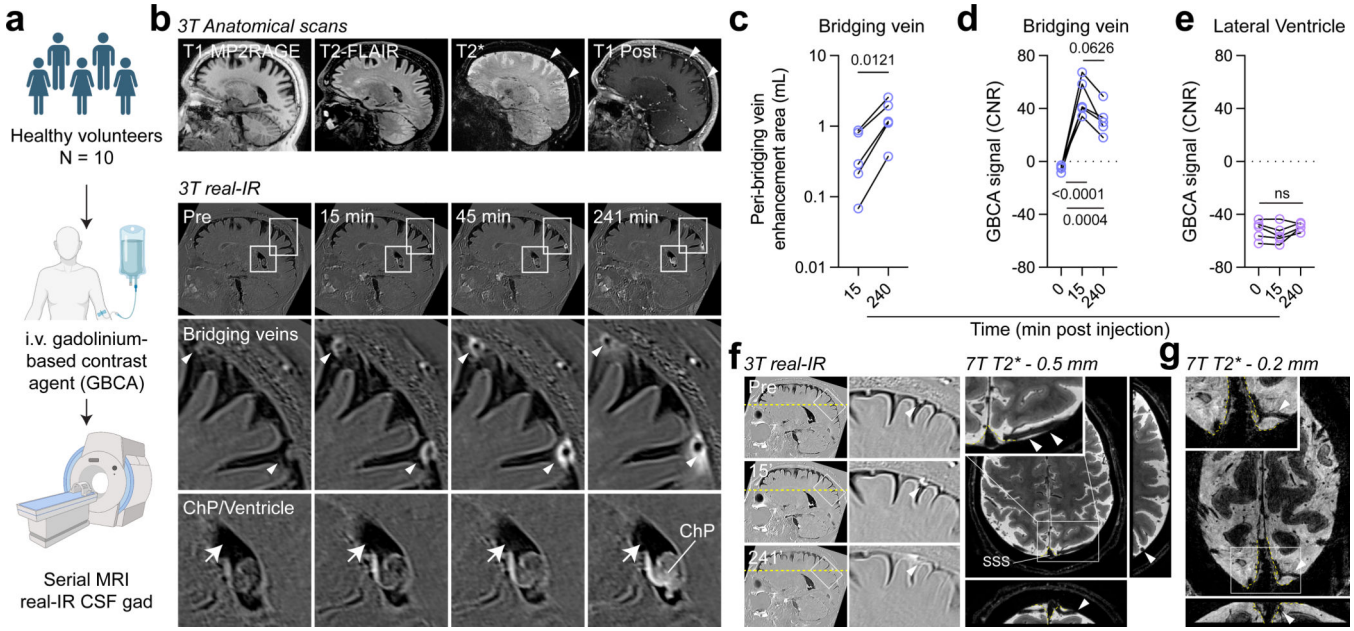

Fig. 4. Enhancement of i.v. tracers around bridging veins in healthy human subjects.

a. Experimental paradigm for examining the influx of i.v. tracers into the CSF of healthy subjects.

b. Sagittal anatomical scans and 3-tesla real-IR scans of CSF gadolinium-based contrast agent (GBCA) enhancement in a healthy adult at baseline, then 15-, 45-, and 240-min post injection.

c. Volume of enhancing areas at 15- and 240-minutes post i.v. GBCA injection. N=5 participants, two-tailed paired t-test.

d. Intensity (contrast to noise ratio, CNR) of enhancing areas around bridging veins at baseline, then 15 and 240 minutes post i.v. GBCA injection. N=5 participants, repeated measures one-way ANOVA with Tukey's post-hoc test.

e. Intensity (contrast to noise ratio, CNR) of the lateral ventricles at baseline, then 15 and 240 minutes post i.v. GBCA injection. N=5 participants, repeated measures one-way ANOVA.

f. Sagittal images of 3-tesla real-IR of a bridging vein showing enhancement and matched 7-tesla T2*-weighted axial and coronal images from the same healthy adult. Arrowheads denote the enhancing vessel. Dashed yellow line in real-IR images shows the plane of the axial scan. Dashed yellow lines on T2*-weighted images denote the boundary between the parasagittal dura and subarachnoid space.

g. Ultrahigh resolution (0.2 mm isotropic) 7-tesla T2*-weighted axial and coronal images of a bridging vein (arrowheads), showing its subarachnoid location as well as its penetration into junction points within the parasagittal dura from the subarachnoid space. Yellow dashed lines denote the boundary between the subarachnoid space and the parasagittal dura.

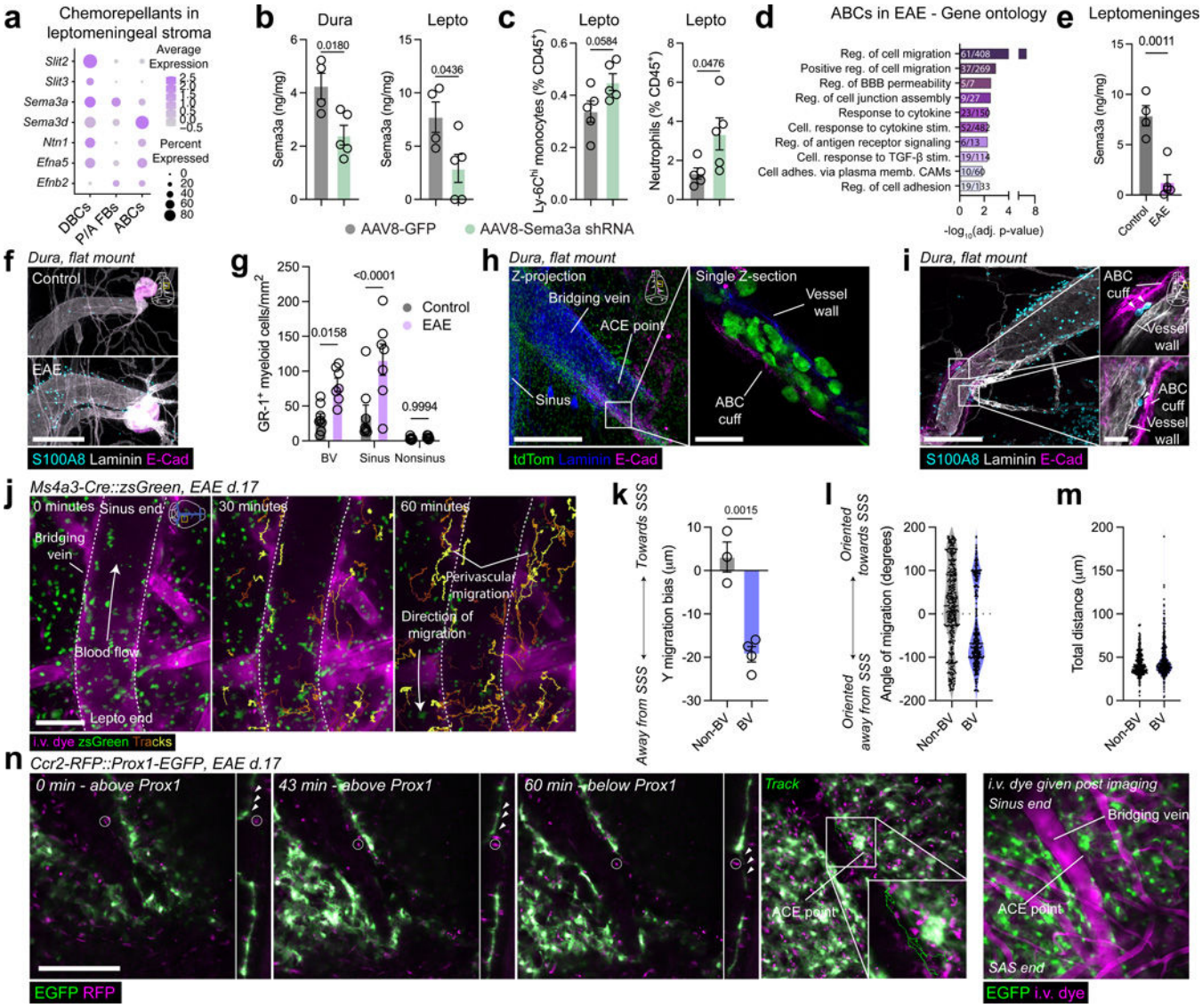

Fig. 5. ACE points permit trafficking of myeloid cells from the dura to the subarachnoid space.

a. Dotplot of the expression of selected chemorepellants in the leptomeningeal stroma, scaled by percentage of cells expressing the gene and expression level. ABC = arachnoid barrier cell, DBC = dural border cell, P/A FB = pial and arachnoid fibroblast.

b. ELISA of Sema3a levels in the dura and leptomeninges of wild type mice 21 days following i.c.m. injection of AAV8-GFP or AAV8-*Sema3a*-shRNA (2×10^{12} GC). Mean ± SEM. N = 4 (AAV8-GFP), 5 (AAV8-Sema3a shRNA) animals, two-tailed, unpaired Student's t-test.

c. Frequency of Ly-$6C^{hi}$ monocytes and neutrophils in the leptomeninges of mice injected with i.c.m AAV8-GFP or AAV8-*Sema3a*-shRNA, 21 days after injection. Mean ± SEM. N = 5 animals, unpaired, two-tailed Student's t-test.

d. Selected significantly enriched gene ontologies in differentially expressed genes (DEGs) in control and EAE ABCs. The number of DEGs as a fraction of the total gene ontology is

given. EAE = experimental autoimmune encephalomyelitis. Enriched gene ontologies were calculated in ENRICHR using the Fisher exact test.

e. Sema3a abundance in leptomeningeal lysates in control and EAE mice at peak of disease. Mean ± SEM. N = 4 (sham control), 5 (EAE) animals, unpaired two-tailed Student's t-test.

f. S100A8-positive neutrophils around bridging veins in the cranial dura at the peak of EAE. Scale = 200 μm.

g. Quantification of the density of GR-1-positive myeloid cells around bridging veins (BV), sinus regions, and non-sinus regions in control and EAE duras. Mean ± SEM. N = 8 (sham control), 7 (EAE) animals, two-way ANOVA with Sidak's multiple comparison adjustment.

h. zsGreen-positive myeloid cells in the space between the ABC cuff and vessel wall of an ACE point in a *Ms4a3*-Cre::zsGreen peak EAE dura. Scale = 200 μm, inset = 10 μm.

i. S100A8-positive neutrophils in the space between the ABC cuff and vessel wall of an ACE point in a peak EAE dura. Scale = 100 μm, inset = 10 μm.

j. *In vivo* two-photon imaging of myeloid cell migration around a bridging vein in *Ms4a3*-Cre::zsGreen monocyte/neutrophil reporter mice at the peak of EAE. Scale = 25 μm.

k. Mean track bias in the Y direction in non-bridging vein and bridging vein regions of *Ms4a3*-Cre::zsGreen monocyte/neutrophil reporter mice at the peak of EAE. Mean ± SEM. N = 3 (non-bridging vein), 4 (bridging vein) regions across 7 animals, unpaired two-tailed Student's t-test.

l. Angle of migration in bridging vein and non-bridging vein regions of *Ms4a3*-Cre::zsGreen monocyte/neutrophil reporter mice at the peak of EAE. N = 3 – 4 animals, each point represents one tracked cell.

m. Total migration distance in bridging vein and non-bridging vein regions of *Ms4a3*-Cre::zsGreen mice at the peak of EAE. N = 3 – 4 animals, each point represents one tracked cell.

n. *In vivo* two-photon imaging of monocyte migration between the dura and subarachnoid space at an ACE point in a *Ccr2*-RFP/*Prox1*-EGFP dual reporter mice at the peak of EAE. Arrowheads indicate the $Prox1^{+}$ layer. Scale = 200 μm.